8-2013

Design, Optimization, and Testing of a Cross-Flow Tidal Turbine

Megan Colleen Swanger

DESIGN, OPTIMIZATION, AND TESTING OF A CROSS-FLOW TIDAL TURBINE

By

Megan Colleen Swanger

B.S. Norwich University, 2006

A THESIS

Submitted in Partial Fulfillment of the

Requirements for the Degree of

Master of Science

(in Mechanical Engineering)

The Graduate School

The University of Maine

August 2013

Advisory Committee:

Michael Peterson, Prof. of Mechanical Engineering, University of Maine, Co-Advisor

Richard W. Kimball, Prof. of Engineering, Maine Maritime Academy, Co-Advisor

Douglas Read, Prof. of Engineering, Maine Maritime Academy

DESIGN, OPTIMIZATION, AND TESTING OF A CROSS-FLOW TIDAL TURBINE

By Megan Colleen Swanger

Thesis Co-Advisors: Dr. Michael Peterson
Dr. Richard Kimball

An Abstract of the Thesis Presented
in Partial Fulfillment of the Requirements for the
Degree of Master of Science
(in Mechanical Engineering)
August 2013

This thesis is a summary of testing conducted with a Darrieus style cross-flow tidal turbine. Many locations around the world have locations suitable for tidal turbine energy, including the Cobscook Bay in Eastport, Maine. Cross-flow turbines are likely to have a smaller impact on the environment compared to axial flow turbines due to their operation at lower tip speed ratios. Since very little experimental data is available presently for cross-flow turbines, this study provides an expansive set of performance data for two NACA series blade profiles of the same chord length. One blade profile was used in two different orientations during testing. The University of Maine tow tank was utilized to perform testing in order to determine the peak power coefficient for each blade profile. Tests of two and four blade turbines were conducted at fixed inflow velocity for a range of tips speeds and blade toe angles. Turbine performance was compared to determine the most efficient solidity ratio and profile. Power coefficient curves compared consistently with previously published data.

Testing was also performed to determine the effects of viscosity and free surface effects by varying water temperature and water column height on turbine performance. This data was collected with the blade profile that provided the most efficient results set to its optimal toe angle. Results determined that both viscous and free surface interactions had considerable effect on efficiency results.

DEDICATION

In loving memory of

Professor Carol E. Stephens, PhD.

Dedicated teacher, mentor, and friend

ACKNOWLEDGEMENTS

I would like to thank my advisor, Dr. Michael "Mick" Peterson, for introducing me to this project and constantly helping me all along the way. I would also like to thank my advisory committee: Dr. Richard Kimball and Dr. Doug Read, for their vast knowledge and guidance. I greatly appreciate the time you all have spent providing input and directing me down the correct path.

I would like to thank Maine Tidal Power Initiative and all of its members for providing such a positive experience that has expanded my knowledge and made me a more conscientious engineer. I'd also like to thank the U.S. Department of Energy for their funding to our project through grant EE-000298, Ocean Renewable Power Company for providing the blades and funding to conduct the experimental tests, Alexander's Welding and Machine for manufacturing the turbine, and the Maine Army National Guard for providing tuition assistance.

I would like to thank the graduate students who worked alongside me: Geoffrey deBree and Matthew Cameron, for developing the experimental test setup, Thomas Lokocz, for designing the blade manufacturing system, and Raul Urbina, for answering my many questions and keeping me focused. I'd also like to thank the undergraduate students that put in countless hours to the project: Thomas McKay, Nathan Rocker, James Staszko, and Kai Whitehead. In addition, I would like to thank Travis Wallace for his generous support and advice during this project.

Finally, I would like to thank my family who has always been supportive of everything I do. I am always ever grateful for your presence in my life.

TABLE OF CONTENTS

LIST OF TABLES

LIST OF FIGURES

LIST OF SYMBOLS

A	Area
A_c	Channel Cross-Sectional Area
A_t	Turbine Cross-Sectional Area
α	Angle of Attack
BR	Blockage Ratio
α_t	Toe Angle
C_p	Power Coefficient
L	Chord Length
d	Water Depth
λ	Tip Speed Ratio
μ	Fluid Dynamic Viscosity
n	Number of Blades
ρ	Fluid Density
R	Turbine Radius
Re	Reynolds Number
σ	Solidity Ratio
T	Rotor Torque
T'	Nondimensional Torque
U_∞	Inflow Velocity
ω	Turbine Angular Velocity
Fr	Froude Number

g	Gravitational Acceleration
F_L	Lift Force
F_D	Drag Force
F_T	Tangential Force
F_N	Normal Force
F_R	Resultant Force
L_D	Turbine Diameter Length
U_R	Relative Fluid Velocity
Fr_p	Froude Number of Prototype
Re_p	Reynolds Number of Prototype
ρ_p	Fluid Density of Prototype
μ_p	Fluid Dynamic Viscosity of Prototype
V_p	Inflow Velocity of the Prototype
L_p	Turbine Diameter Length of the Prototype
Fr_m	Froude Number of Model
Re_m	Reynolds Number of Model
ρ_m	Fluid Density of Model
μ_m	Fluid Dynamic Viscosity of Model
V_m	Inflow Velocity of Model
L_m	Turbine Diameter Length of Model

LIST OF ABBREVIATIONS

ASCII	American Standard Code for Information Interchange
ARC	Aquaculture Research Center
EIA	Energy Information Administration
LE	Leading Edge
MHK	Marine Hydrokinetics
NACA	National Advisory Committee for Aeronautics
ORPC	Ocean Renewable Power Company
TSR	Tip Speed Ratio
TE	Trailing Edge

CHAPTER 1

INTRODUCTION

1.1 General

Around the world, countries have started to make the transition to renewable energy. In the United States, the President has proposed an aggressive goal of generating 80% of our electricity from clean energy sources including tidal power by 2035. Since 2008, renewable energy generation has been steadily on the rise in the U.S., as seen in Fig 1.1.

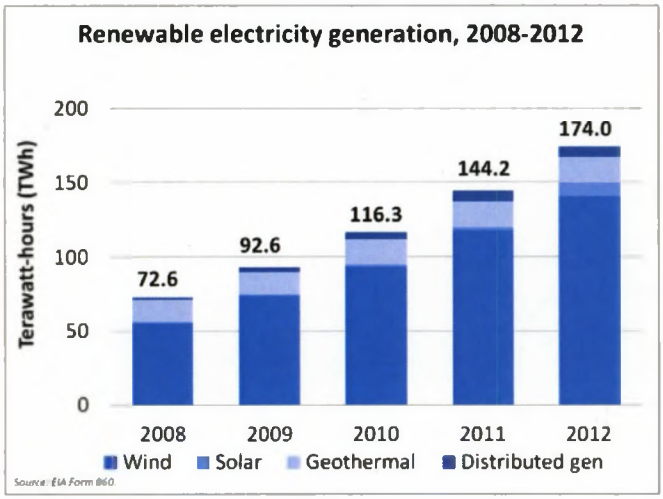

Figure 1.1 - Renewable electricity generation for the United States from 2008-2012 (EIA, 2011)

Although ocean energy is not a continuous source of power, it is extremely reliable, changing direction every six hours. The United States consumes approximately 4,000 terawatt hours (TWh) of electricity each year. The Department of Energy estimates the waves and tidal currents around the United States have the potential of generating a

maximum of 1,420 TWh which is more than a third of the total U.S. annual electricity consumption (DOE, 2012). The purpose of this thesis is to present experimental data in order to provide useful information to implement and expand the use of marine hydrokinetic (MHK) turbines.

1.2 Tidal Power Harnessing

Tidal power is typically harnessed in one of three ways: tidal barrage, tidal fence, or tidal turbine. Tidal barrages are dam-like constructions that stretch out across an inlet to collect tidal water through sluice gates during the incoming high tide (Fig. 1.2). The water is stored in a basin until the water empties through turbines on the ebb tide. Although tidal barrages are efficient sources of tidal energy, they place a large impact on the environment in which they are emplaced.. Both species migration and navigation can be impeded by barrages. Turbidity and salinity of the water can also be affected, changing the overall ecosystem.

Figure 1.2 – The second largest tidal barrage in the world, La Rance Tidal Power Plant, located in Brittany, France. (Image source: http://www.energybc.ca/profiles/tidal.html)

Tidal fences are typically installed by mounting vertical axis turbines in a channel resembling large turnstiles. They are not as obstructive as a barrage, but may still impact the movement of larger marine animals and generally have a lower power output. Some researchers found that the fences could be designed with space between the caisson wall and rotor to allow fish to safely pass (Pelc, Fujita, 2002).

Tidal turbines are most commonly designed in either axial or cross-flow configurations. Axial flow turbines, although more efficient than cross-flow turbines, may be more harmful to marine life due to operation at higher tip speed ratios (TSR). Tip speed ratio, λ, as described in Eq. 1.1, is a non-dimensional value for characterizing operational turbine speed where R is the turbine radius, ω is the turbine angular velocity, and U_∞ is the inflow velocity. Axial flow turbines typically operate at a TSR range from 5 to 7 for maximum efficiency (Lokocz, 2012).

$$\lambda = \frac{R\omega}{U_\infty} \tag{1.1}$$

Cross-flow turbines have many desirable qualities despite having a lower efficiency than the axial design. One major difference is that the cross-flow turbine rotates in a constant direction independent of the direction of flow, simplifying the issue of reorienting the turbine during the change of tides which is necessary for axial flow turbines. Another advantage is that maximum efficiency is obtained at TSR much lower than axial turbines (around 1 to 2 TSR) thus reducing the risk to marine life in terms of mechanical strike (Polagye et al., 2010). One example of a cross-flow turbine in implementation, produced by Ocean Renewable Power Company (ORPC), can be seen in Fig. 1.3.

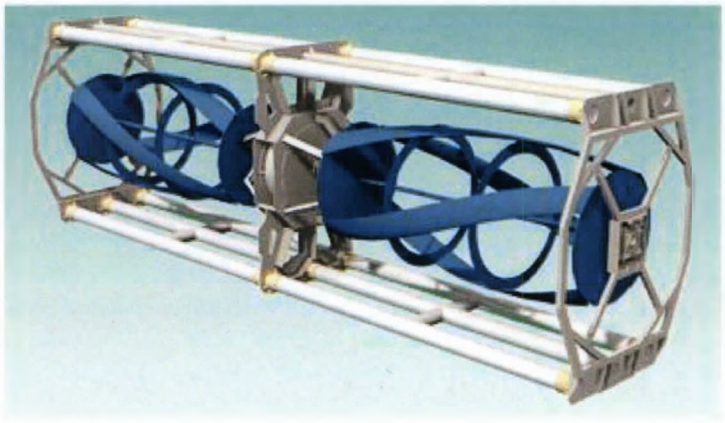

Figure 1.3 – Model of Ocean Renewable Power Company's cross-flow turbine generator unit. (Image source: http://orpc.co/orpcpowersystem_turbinegeneratorunit.aspx)

1.3 Mechanical Geometry and Technical Definitions

1.3.1 Turbine Geometry

The Darrieus style turbine was chosen for the acquisition of the data set presented in this thesis. This simple design used straight blades arranged horizontally and parallel to the central axis of the turbine as seen in Fig. 1.4.

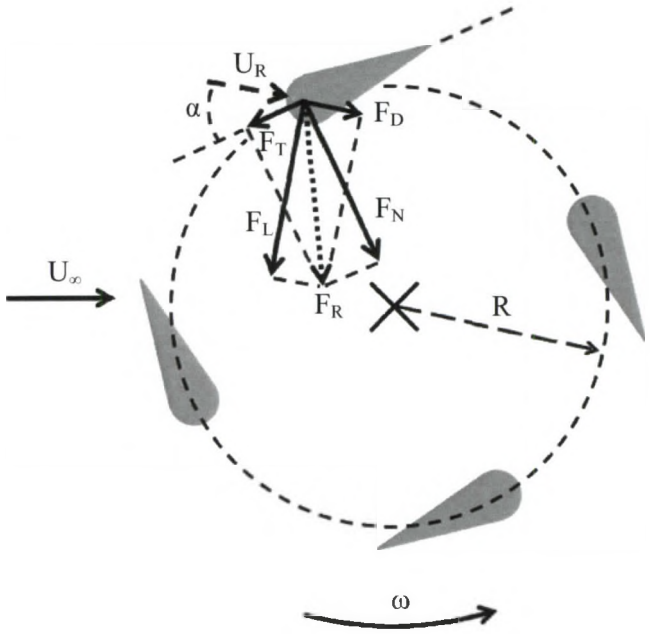

Figure 1.4 – Side view of a Darrieus style turbine used in this testing. The variable R is the turbine radius, ω is the angular velocity of the turbine, U_∞ is the inflow velocity of the water, α is the angle of attack, U_R is the relative velocity vector, F_D is the drag force, F_L is the lift force, F_R is the resultant force of the lift and drag forces, and F_T and F_N are the components of F_R that are tangential and normal to the chord length. (deBree, 2012)

For operation of this turbine, water passes through the turbine at an inflow velocity, U_∞, which rotates the blades around the central axis. As the blades turn lift and drag forces on the blades produce torque. When the average torque for a revolution is positive, power is generated by the turbine. For cross-flow turbines, it is mostly the lift forces that produce the power in the system. To obtain the maximum lift, the blades can be mounted at different angles and be manufactured to have a camber, or bend, to obtain more power. This thesis will explore the effects of toe angle and camber to determine the optimal setup. Toe angle is defined as zero degrees when blades are mounted with the chord length perpendicular to the radius and the leading edge oriented toward the direction of rotation (Fig. 1.5).

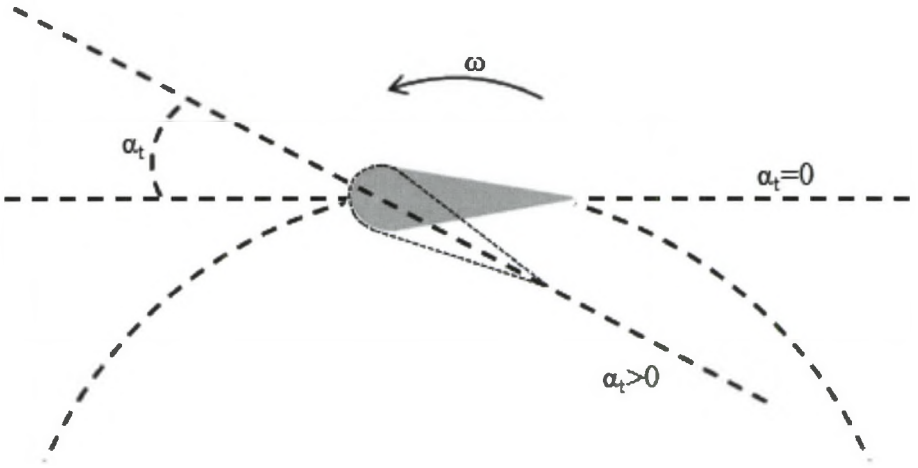

Figure 1.5 – Diagram of the side view of the turbine to identify how toe angle, α_t, is determined and referenced. The grey shaded foil is mounted where the toe angle is zero. The dashed outlined foil shows how the blade orientation could be changed to acquire a positive toe angle.

1.3.2 Blade Geometry

Straight blades in the cross-flow turbine can be manufactured in many different ways that can improve the overall turbine performance. Blade characteristics that are integral in cross-flow optimization include the blade shape, number of blades, and chord length. These characterizations determine the solidity of the turbine, which is a ratio measurement of the blade area to the swept area of the blade (Shiono et al., 2000). The solidity ratio, σ, is calculated through Eq. 1.2, where n is the number of blades, L is the blade chord length, and R is the turbine radius. Most documented research has shown testing with a solidity ratio between approximately 0.1 and 0.5. Testing outside this range has a significantly decreased efficiency of 10% or less.

$$\sigma = \frac{nL}{2\pi R} \tag{1.2}$$

An example of a blade profile in Fig. 1.6 depicts the chord length, which extends from the leading edge (LE) of the blade to the trailing edge (TE) of the blade. Other important blade dimensions include blade thickness, camber line, and camber.

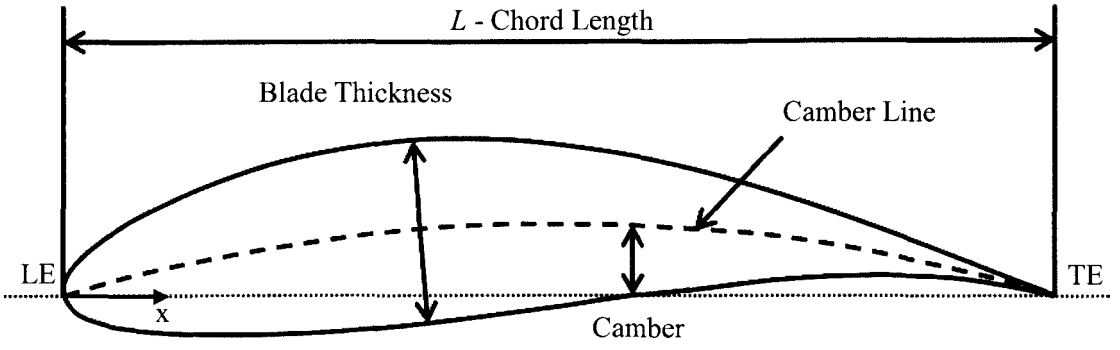

Figure 1.6 - An example of a straight blade profile for a cross-flow turbine. Geometry includes chord length, leading edge (LE), maximum thickness, maximum camber, camber line, and trailing edge (TE).

The turbine rotates in the direction of the leading edge. The distance between the leading edge and trailing edge is the chord length. Blade thickness changes along the length of the chord length. In this figure the blade has a slight curve which labels it as a cambered or asymmetric blade. Blades that lack this camber shape are termed symmetric blades. The midpoint of the upper and lower halves of the foil is the camber line. The distance from the camber line to the x-axis is the camber. Typically, the maximum camber is referenced when identifying blade characteristics (Nakayama, 1998).

This turbine apparatus has been tested with many different types of blades. The first testing by Bates (2010) included wooden blades. These foils were upgraded by manufacturing 3-D printed plastic blades and carbon fiber blades (Lokocz, 2010). Testing by deBree showed that although the carbon fiber blades were much more rigid

than the 3-D printed plastic blades, there was negligible difference in their performance, varying by only 0.3%.

1.3.3 Effects of Lift, Drag, and Angle of Attack

The elements of lift and drag can change greatly depending on the angle of attack of the blades, therefore increasing or decreasing the overall efficiency of the turbine. Angle of attack is defined as the angle between the chord line and the relative velocity vector as seen in Fig. 1.7 where F_L is the lift force and F_D is the drag force. In general, the lift coefficient and drag coefficient are both zero at an angle of attack of zero degrees for symmetrical blades. As the angle of attack increases, so does the lift coefficient until maximum lift is reached and stall occurs. The drag coefficient increases to the stall point as well, but not to the magnitude of the lift coefficient. After the stall point, the drag coefficient increases rapidly and turbine performance is not easily predictable. When using cambered blades, the angle at which the lift coefficient is zero changes.

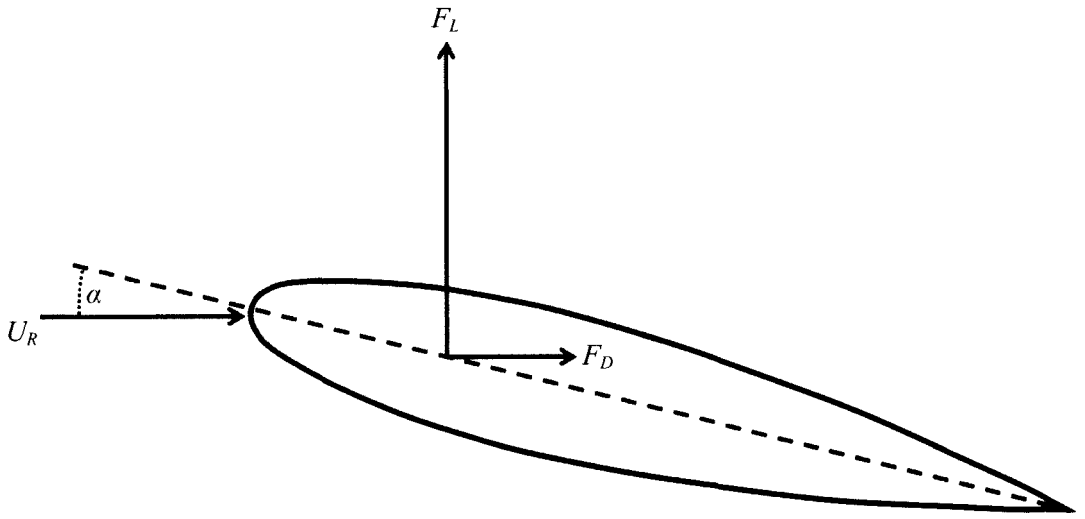

Figure 1.7 – Representation of lift and drag forces on a symmetrical blade at a positive angle of attack. F_L is the lift force, F_D is the drag force, α is the angle of attack, and U_R is the relative velocity of the fluid.

1.3.4 Performance Characteristics

For cross-flow turbine designs, there are several parameters that can be used to describe the performance characteristics. Tip speed ratio, as mentioned earlier in this chapter, describes the ratio of angular velocity of the turbine to the inflow velocity. Another parameter, the power coefficient, describes the overall efficiency of the turbine. It is the main focus in turbine design. The power coefficient is calculated by comparing the power produced by the turbine to the maximum possible power available for a fluid at a given velocity moving through a cross sectional area of the turbine (Eq. 1.3). In this equation, T is the instantaneous torque, ω is the angular velocity of the turbine, ρ is the density of the fluid, A_t is the cross sectional area of the turbine, and U_∞ is the inflow velocity. The power coefficient is averaged for each instantaneous torque value to find the overall average power coefficient for a certain TSR and inflow velocity.

$$C_p = \frac{T\omega}{\frac{1}{2}\rho A_t U_\infty^3} \tag{1.3}$$

Another parameter that is used in turbine design is the nondimensionalized torque, which can be used to estimate loads on a full scale turbine. In Eq. 1.4, nondimensionalized torque, T', is defined where T is the rotor torque, ρ is the density of the fluid, A_t is the cross sectional area of the turbine, R is the radius of the turbine, and U_∞ is the inflow velocity.

$$T' = \frac{T}{\frac{1}{2}\rho A_t R U_\infty^2} \tag{1.4}$$

To calculate the nondimensional torque for experimental testing, the data was bin-averaged to determine the nondimensional torque as a function of angular position.

1.4 Model Scaling

Variations in Reynolds number affect the lift and drag produced. As the Reynolds number increases the effect of Reynolds number variations on the lift and drag coefficients decreases. Reynolds number is a parameter that can be used to scale turbine devices (Eq. 1.5).

$$Re = \frac{\rho U_\infty L_D}{\mu} \tag{1.5}$$

In this equation, ρ is the density of the fluid, U_∞ is the fluid reference velocity, L_D is the reference length, and μ is the dynamic viscosity of the water. For this thesis, the fluid reference velocity was the inflow velocity and the length reference was the turbine diameter. In many cases, experimental testing has found that limitations in flow velocity prohibit replications of full scale Reynolds number conditions (McAdam et al., 2009). As a result, Froude number scaling is commonly used instead of Reynolds number scaling. Both cannot be scaled at the same time since Reynolds number relies on a velocity-length product while Froude number is dependent upon velocity divided by square root of the length. For proper Reynolds number scaling, the inflow velocity would have to increase as the size of the model decreased which becomes inhibitive when designing experimental tests on a model. Since the model in this study is more than ten times smaller than the prototype, velocities would need to be upwards of 23m/s to ensure dynamic similitude, which is not possible in a typical tow tank.

In this study, the Froude number was used to verify scaling parameters, which provides a conservative amount of power produced in testing since a lower Reynolds number in model testing would reduce turbine performance compared to the full scale prototype (McAdam et. al, 2009). The Froude number, Eq. 1.6, relates the inflow velocity, U_∞, to the square root of gravitational acceleration, g, and the turbine diameter, L_D. Eq. 1.7 relates how the scale model and prototype compare in terms of dynamic similitude, where the Froude numbers of the scale model, denoted with subscript *(m)*, and prototype, subscript *(p)* are equal.

$$Fr = \frac{U_\infty}{\sqrt{gL_D}} \tag{1.6}$$

$$\frac{U_{\infty(m)}}{\sqrt{gL_{D(m)}}} = \frac{U_{\infty(p)}}{\sqrt{gL_{D(m)}}} \tag{1.7}$$

In this thesis, the model is the cross-flow turbine located at the University of Maine tow tank. The model is being compared to the dimensions of Ocean Renewable Power Company's cross-flow turbine located in the Cobscook Bay in Eastport, Maine (Fig. 1.8). With the model operating at an inflow velocity of 2.62 ft/s, the model was properly Froude scaled to the prototype. See Appendix A for scaling calculations.

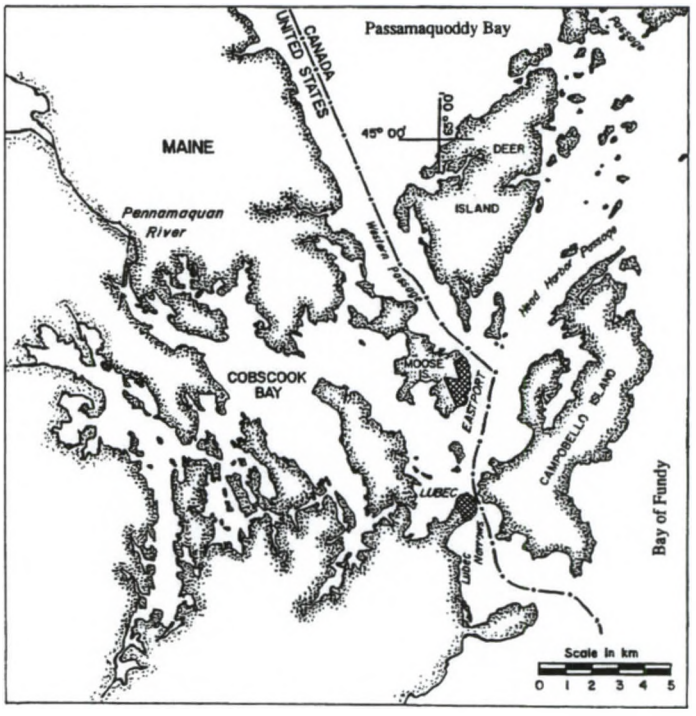

Figure 1.8 – The Cobscook Bay in Eastport, Maine where Ocean Renewable Power Company installed their TidGen™ Power System. Information specific to this setup was used for scaling purposes. (Image source: www. http://rocky.umeoce.maine.edu/xdy/cobscook/plot/cobscook1.jpg)

1.5 Thesis Overview

This thesis provides a detailed data set for two and four-bladed cross-flow turbines. Two different blade profiles were used at varying toe angles to compile an extensive set of data. The first profile chosen was the NACA 0018, a symmetrical blade with 3.5" chord length. The second profile, NACA 4418, was selected due to its similarities to the NACA 0018. The NACA 4418 has the same chord length and thickness as the NACA 0018, but has a slight camber equal to 4% of the chord length. The NACA 4418 was also tested in the reverse camber orientation, which will be discussed in a later chapter.

The objective of this thesis was to explore several hypotheses that would determine the optimal parameters for cross-flow turbine operation. The first hypothesis was that two-blade symmetrical foil turbines are more efficient than four-blade symmetrical foil turbines. The next study involved the comparison of the symmetrical foils with the cambered foils. Since the symmetrical and cambered foils have the same chord length, the solidity ratio remained constant in both sets of data. The results from this study led into the final hypothesis, which anticipated that the symmetrical blades would be more efficient than both the cambered and reverse cambered blades.

CHAPTER 2

EXPERIMENTAL TEST METHODS

2.1 Experimental Setup

2.1.1 Facility

Experimental testing was executed at the University of Maine tow tank at the Aquaculture Research Center (ARC) (Fig. 2.1). The tank is 100 feet long, 8 feet wide, and has a maximum depth of 3.5 feet (Fig. 2.2). The turbine was mounted to an aluminum carriage resting on steel rails running the length of both sides of the tow tank. The carriage measured 4 feet long, 8 feet wide, and 1 foot high and moves along the rails by a wire wound around a drum powered by an AC motor. The carriage is powered by an extending cable that is hung from a track attached to the ceiling. On the front of the carriage, a beam is fixed to allow attachment and detachment of the turbine as needed (Fig 2.3).

Figure 2.1 – University of Maine tow tank located at the Aquaculture Research Center

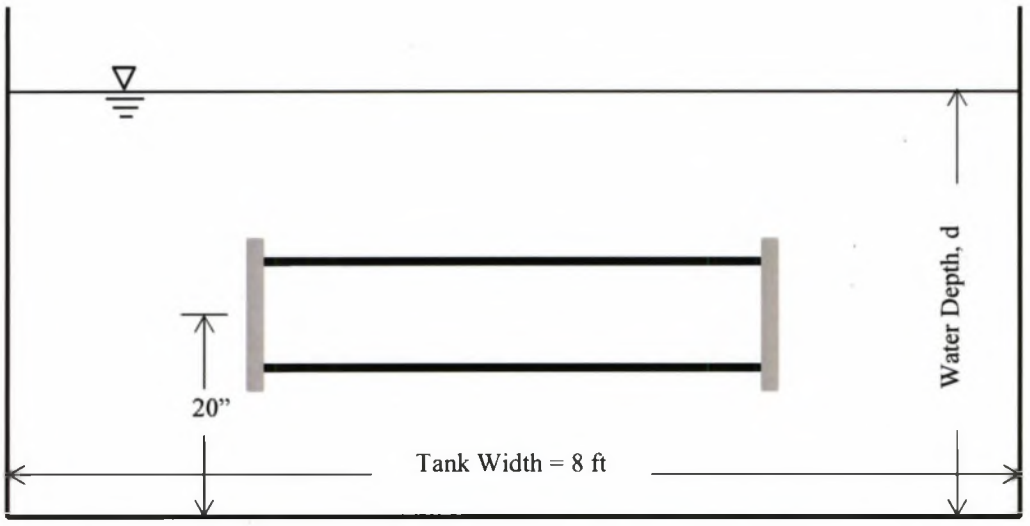

Figure 2.2 – Cross-sectional schematic of the tow tank and turbine router. Tank width and distance from the center of the turbine to the bottom of the tank remained constant for all testing. The turbine is centered along the tank width. Water depth, *d*, was 40 inches for all testing with the exception of the varying depth study where water depth ranged from 30 inches to 44 inches.

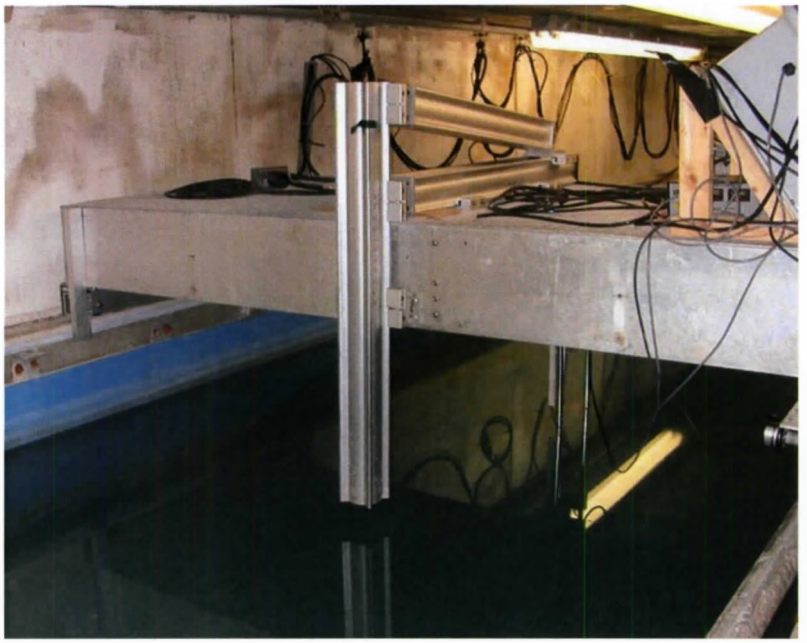

Figure 2.3 – Turbine beam mount on tow tank carriage at the University of Maine tow tank at the Aquaculture Research Center (ARC)

2.1.2 Apparatus

Originally designed by Bates (2010) and later upgraded by deBree (2012) and Cameron (2012), the turbine is designed to allow for expedient adjustment or changing of blades. Currently, the end plates allow the turbine to be set up in two and four-blade configurations with blades spanning 30 inches (Fig. 2.3). Angle indicators were designed along with indicator alignment holes to provide an easy method of adjusting the toe angle from -10^0 to $+10^0$ with one degree increments from -10^0 to -7^0, half degree increments from -6.5^0 to $+3^0$, and one degree increments from $+3^0$ to $+10^0$. Toe angles were verified using the Coordinate Measuring Machine (CMM). By removing the angle indicators, the blades can be removed, added, or swapped out with a new profile quickly and easily.

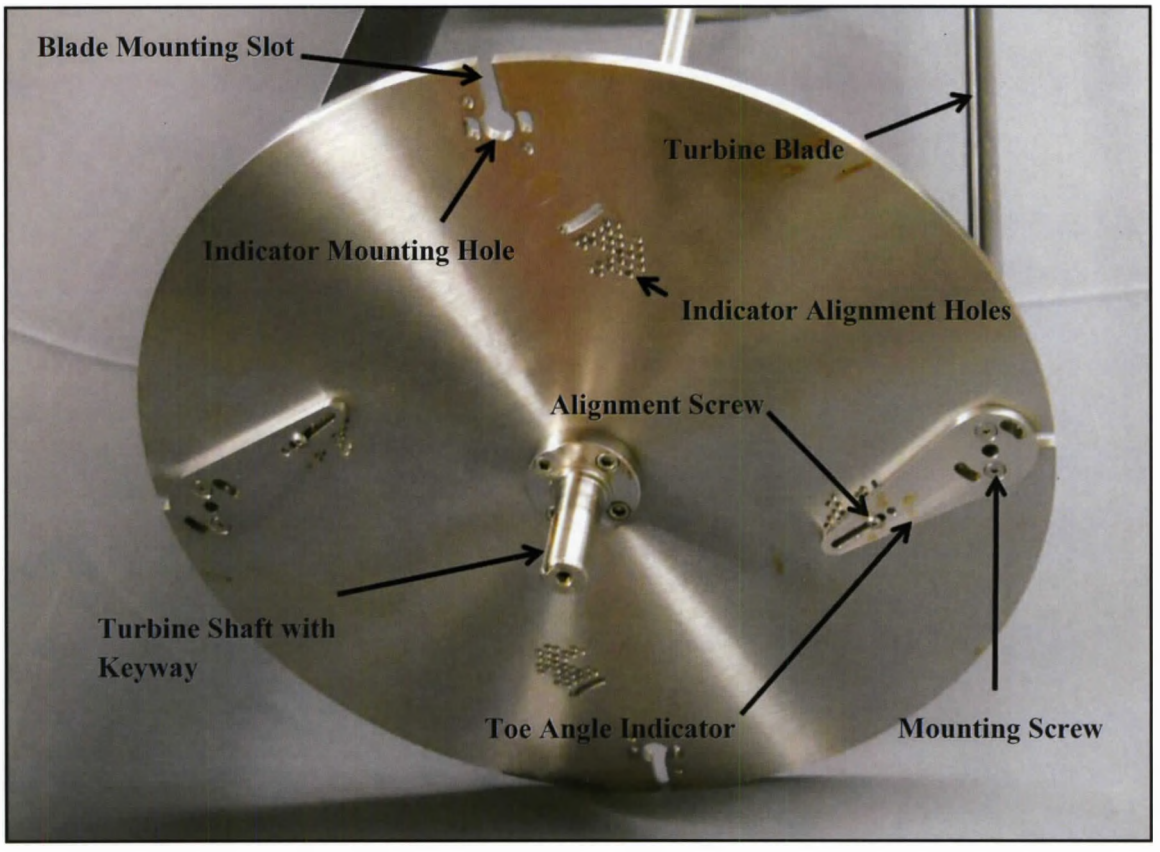

Figure 2.4 – Turbine endplate with attached angle indicators and blades (deBree, 2012)

2.1.3 Operation

The turbine operated with a motor and controller coupled with a gear head mounted to a rectangular box tube that provided support to the turbine. The gear head was connected to a drive train which rotated the turbine via chain drive that extended down to the turbine rotor through aluminum shrouds. All operation was conducted by remote desktop connection from a laptop to the onboard carriage computer.

LabView was utilized to control operation of the system through a program originally developed by Bates (2010), then upgraded by deBree (2012) and Cameron (2012). The program allowed input variables of inflow velocity and TSR. Other inputs to the system were controlled mechanically to include water column height, turbine height in the water column, toe angle, and the number of blades. Water column height was controlled by adding or draining water from the tow tank, turbine height was adjusted by moving the turbine up or down on the beam mount, and toe angle was adjusted and blades were added or removed from the endplates.

For all experimental testing, the following inputs were held constant: water column height, turbine height in the water column, and inflow velocity or carriage velocity. For the purpose of clarity, a 'test set' refers to a complete group of data for a certain blade profile and solidity at a range of toe angles. Each test set was organized in a test matrix (Appendix B) to define the range of TSR in order to capture the peak efficiency.

2.2 Measured Values

During each test run, the time, turbine angular velocity, and inflow velocity were measured along with the turbine torque to determine the efficiency of the turbine. Time

was recorded by a sampling rate clock. Turbine angular velocity was measured using a position encoder attached to the driveshaft by filtering the signal (Appendix E) and differentiating with respect to time from the gathered data. Inflow velocity was measured using a position encoder similar to the turbine encoder. Again, position was measured, the signal was filtered, and the data differentiated with respect to time. Turbine torque was measured using a load cell attached to the rectangular box tube, while the thrust data was collected using two horizontal load cells opposite the torque load cell (Fig. 2.4).

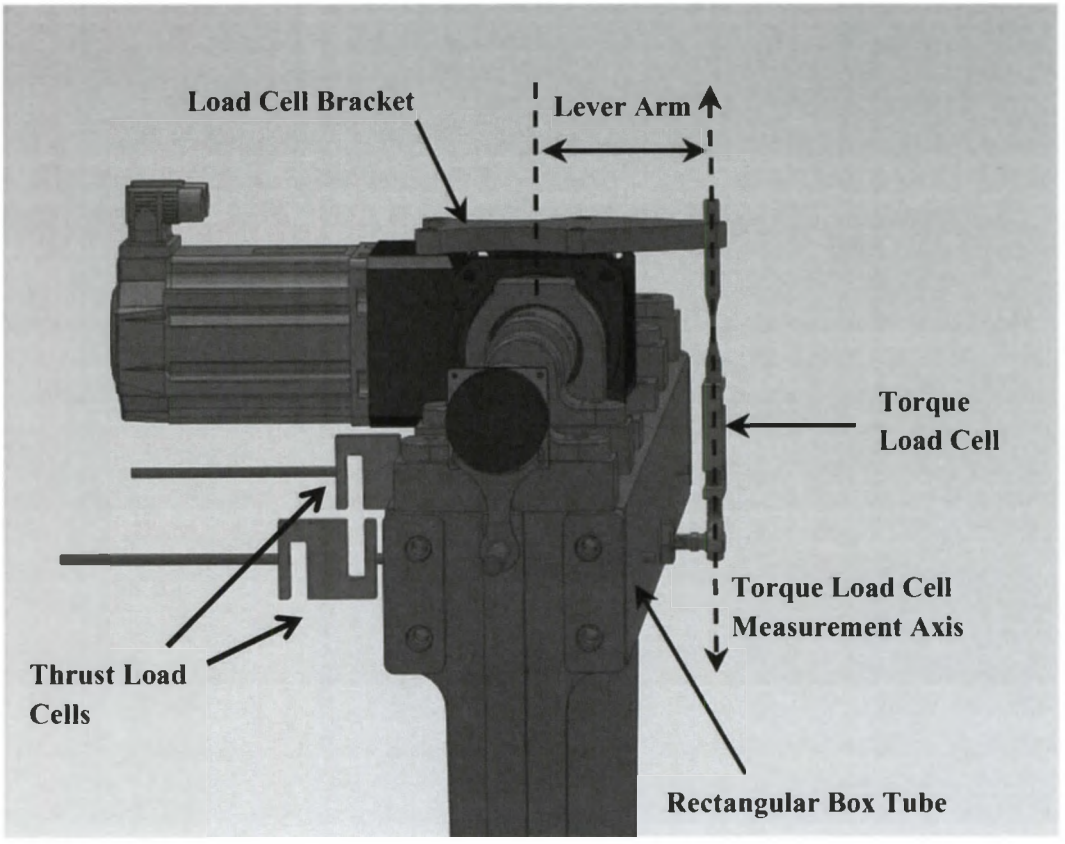

Figure 2.5 – Model of the turbine motor, rectangular box tube, torque load cell, thrust load cells, and turbine encoder.

2.3 Experimental Test Methods

2.3.1 Preliminary Tests

Prior to the execution of each test set, several preliminary tests were performed to ensure accuracy of the system. The first test was to determine the uncertainty in the data. With the turbine attached to a dry mount outside of the water, known weights ranging from 0 to 18.14 kg were added to the turbine motor at a fixed distance from the turbine rotational axis. Each weight corresponded to an applied torque as determined by Eq. 2.1 where T is the applied torque, F is the force on the load cell, and l is the length of the lever arm.

$$T = Fl \tag{2.1}$$

The torque load cell output was a linear function of the load applied, so the slope and offset were found by using a linear regression. From the slope and intercept error the uncertainty was determined. To calculate the error, the output was used from a weight just heavier than the load for an actual test run (0.374 N). This was multiplied by the lever arm of the applied load to determine the error of the torque from the force measurement, which was 0.0726 N·m (deBree, 2012).

Another important preliminary test was to determine the friction torque and end plate drag. To find the friction, the turbine was rotated out of the water on a dry mount. Operating the turbine at a variety of rotational speeds, the torque and angular velocity were determined and plotted as seen in Fig. 2.5.

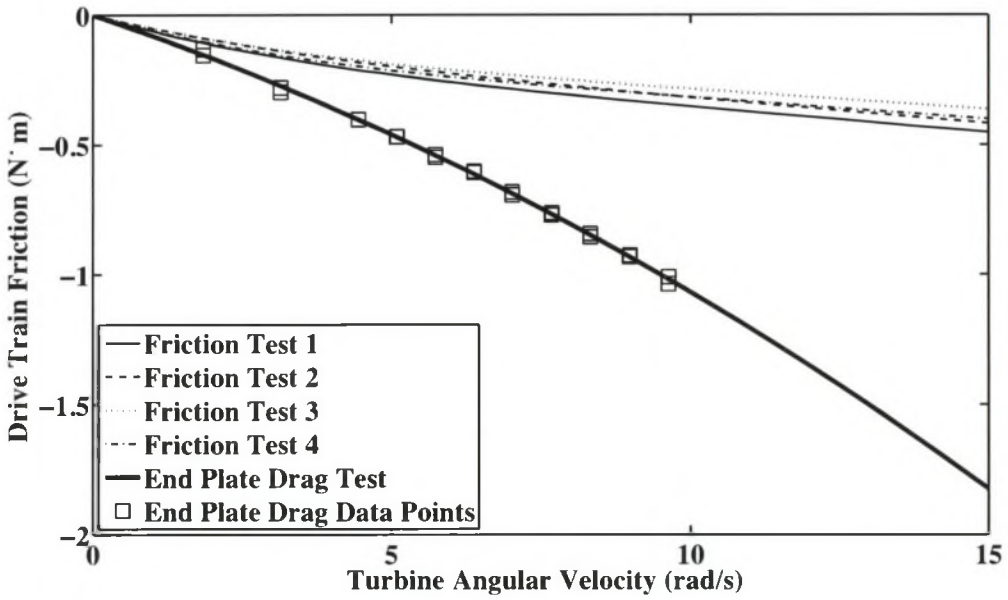

Figure 2.6 - Drive-train friction and end plate drag curves as a function of turbine angular velocity. Drive-train friction curves were obtained outside the tow tank on the dry mount post, while end plate drag tests were performed inside the tank. Both tests were performed with blades removed and center bar mounted (deBree, 2012). The center bar, with a diameter of only 0.01905 m, had a drag force of 1.39 N and was therefore determined to be negligible in the calibration.

The end plate drag was the final preliminary test before performing test matrix data collection. The blades were removed and a bar was installed in the center of the turbine. With this setup, tests were performed at an inflow velocity of 0.8 m/s at the same TSR range as identified in the test matrix about to be run. The data was analyzed and plotted as the end plate drag curve (Fig. 2.6).

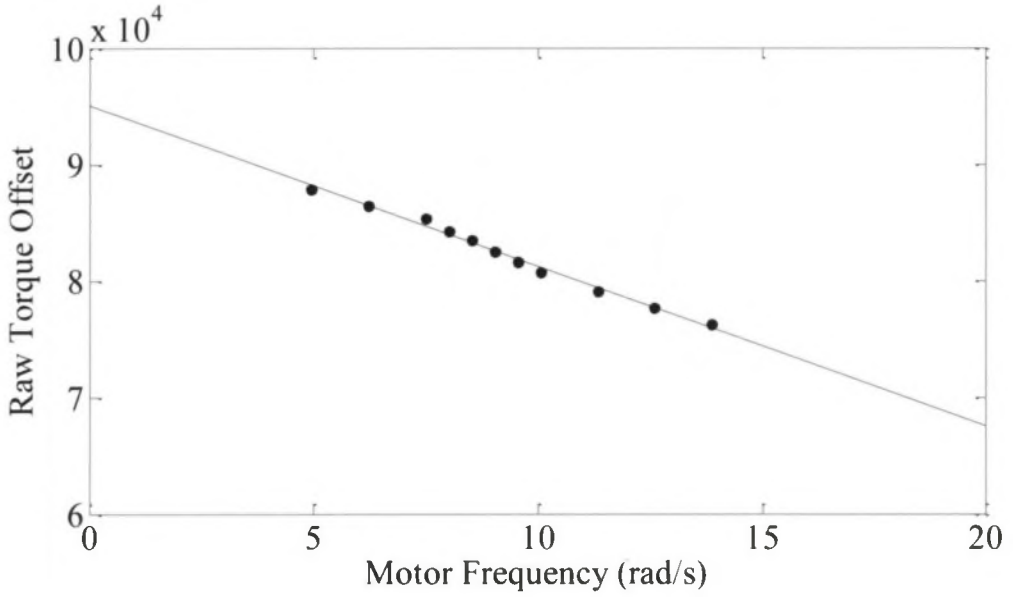

Figure 2.7 – End plate drag curve as a function of motor frequency.

2.3.2 Experimental Testing Procedure

Each test set was organized and listed in a test matrix (Appendix B) to define the TSR for each toe angle and blade profile. The bar was removed from the center of the turbine and the blades were installed. The torque offset was determined by rotating the turbine slowly to find the preload on the torque load cell. The mean torque of the torque load cell was then used for the analysis of the data in the test set by establishing the preload on the system.

For each experimental test, the carriage was accelerated down the length of the tank to the specified velocity and TSR with the turbine attached to the turbine beam mount on the carriage. For all testing, the length of each run was set to 65 feet. The data started recording after the acceleration period at a sampling rate of 2 kHz. Data was written to a binary file during the test, and then converted to ASCII once the test run is complete.

Each power coefficient curve corresponds to a single toe angle where individual points represent an experimental test at a single TSR.

CHAPTER 3

SYMMETRICAL FOIL RESULTS

The symmetrical NACA 0018 foils were tested in two and four-blade configurations at multiple toe angles. Power coefficient curves were compared for each setup to find the peak efficiency and optimal toe angle. The goal of this comparison was to determine if a lower solidity turbine was more efficient than higher solidity turbines, similar to testing performed by Shiono et al. (2000).

3.1 Geometry of NACA 0018 Blades

The symmetrical profile of the NACA 0018 blade is shown in Fig. 3.1. The blades used in the testing had a 3.5 inch chord length. This blade design, and similar symmetrical profiles, such as the 0009, 0012, and 0015 used by Sheldahl and Klimas (1981), are commonly used in Darrieus vertical axis wind turbines (VAWT).

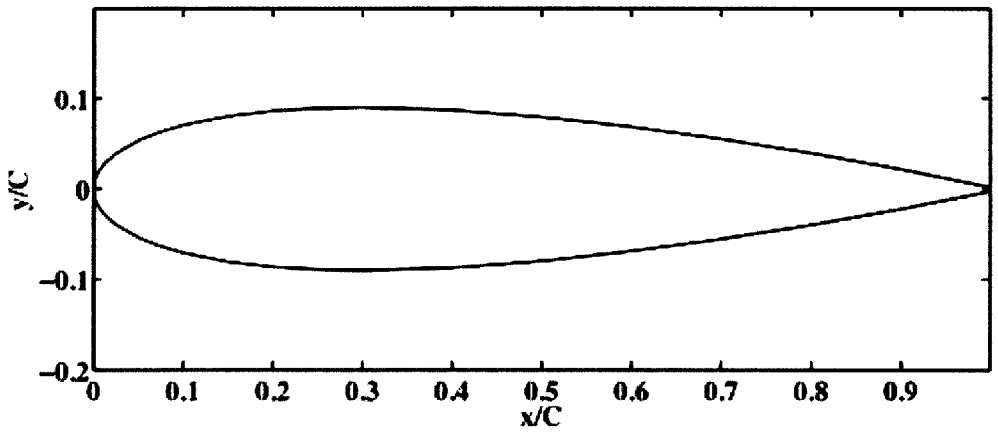

Figure 3.1 – Profile view of the symmetrical NACA 0018 blade

3.2 Two-Blade Test Results

Two-blade tests were conducted at toe angles from -3^0 to $+10^0$ in increments of one degree. Inflow velocity for all testing was set at 0.8 m/s with the turbine centered in the water column, which had a temperature of 67^0F. With a solidity ratio of 0.171, it was estimated that the max power coefficient would be reached at a TSR between 1.6 to 2, based on experimental solidity data by Shiono et al. (2000). As a result, testing was done at a TSR range from 1 to 2.75 to ensure the peak was acquired.

The maximum power coefficient of 42.4% occurred at the $+6^0$ toe angle at a TSR of 1.6 as seen in Fig. 3.2 through 3.5. The $+6^0$ and $+5^0$ toe angles had very similar efficiency curves, varying at peak C_p by only 0.4% and no more than 2% in other parts of the curve. The results show that the efficiency increases steadily from -3^0 toe angle to the peak at $+6^0$. From toe angles of $+7^0$ to $+10^0$, although the efficiency decreases it does not decrease steadily, most likely due to blade stall after maximum lift is reached. Sheldahl and Klimas (1981) performed experimental testing for the lift and drag coefficients of the NACA 0018 blades at varying angle of attack that show this peak in the lift coefficient (Fig. 3.6).

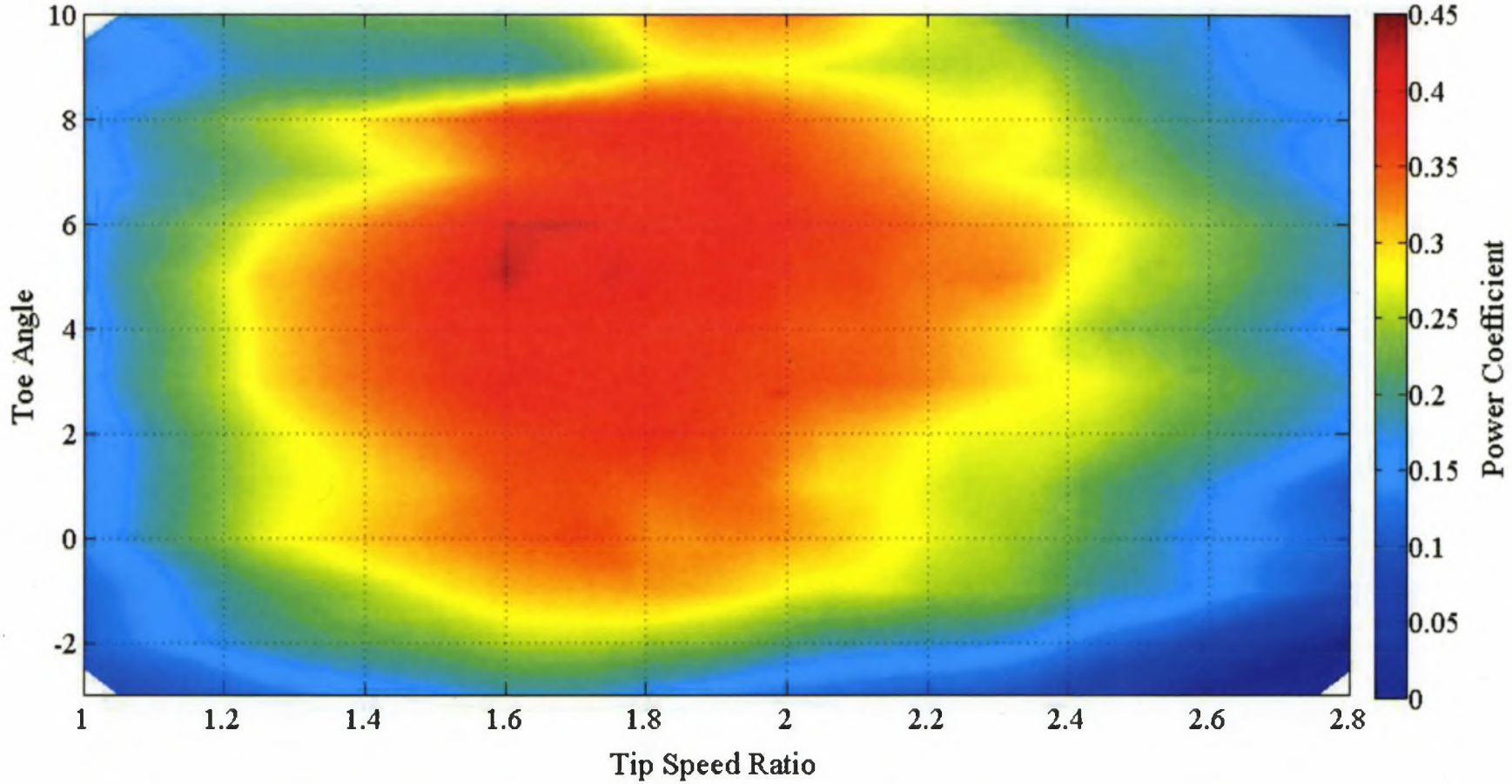

Figure 3.2 – Power coefficient contour plot for two-blade testing of 3-D printed NACA 0018 blades with solidity ratio $\sigma = 0.171$ and inflow velocity $U_\infty = 0.8$ m/s.

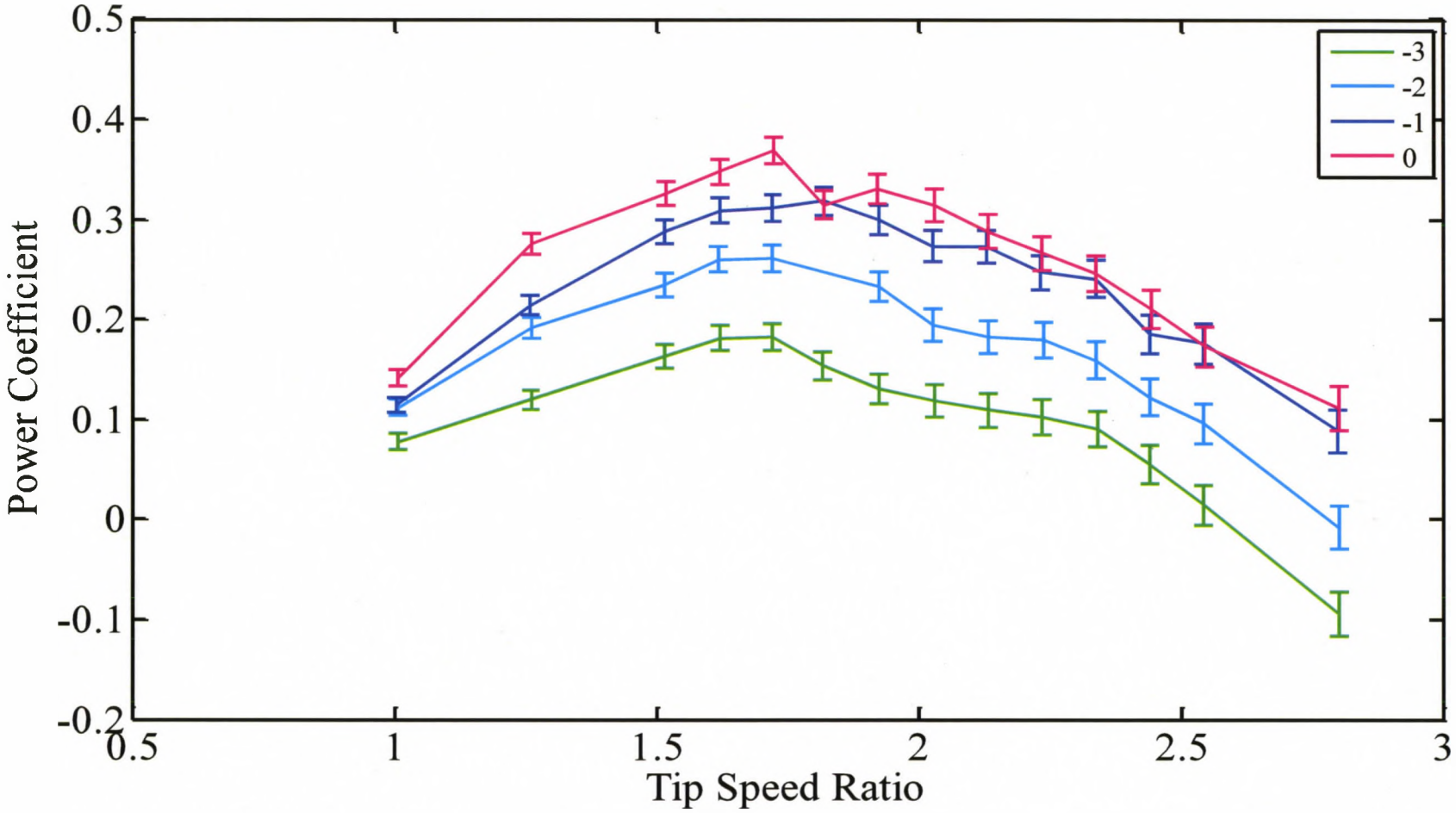

Figure 3.3 – Power coefficient curves for two-blade testing of 3-D printed NACA 0018 blades from toe angles from -3° to 0° with solidity ratio $\sigma = 0.171$ and inflow velocity $U_\infty = 0.8$ m/s.

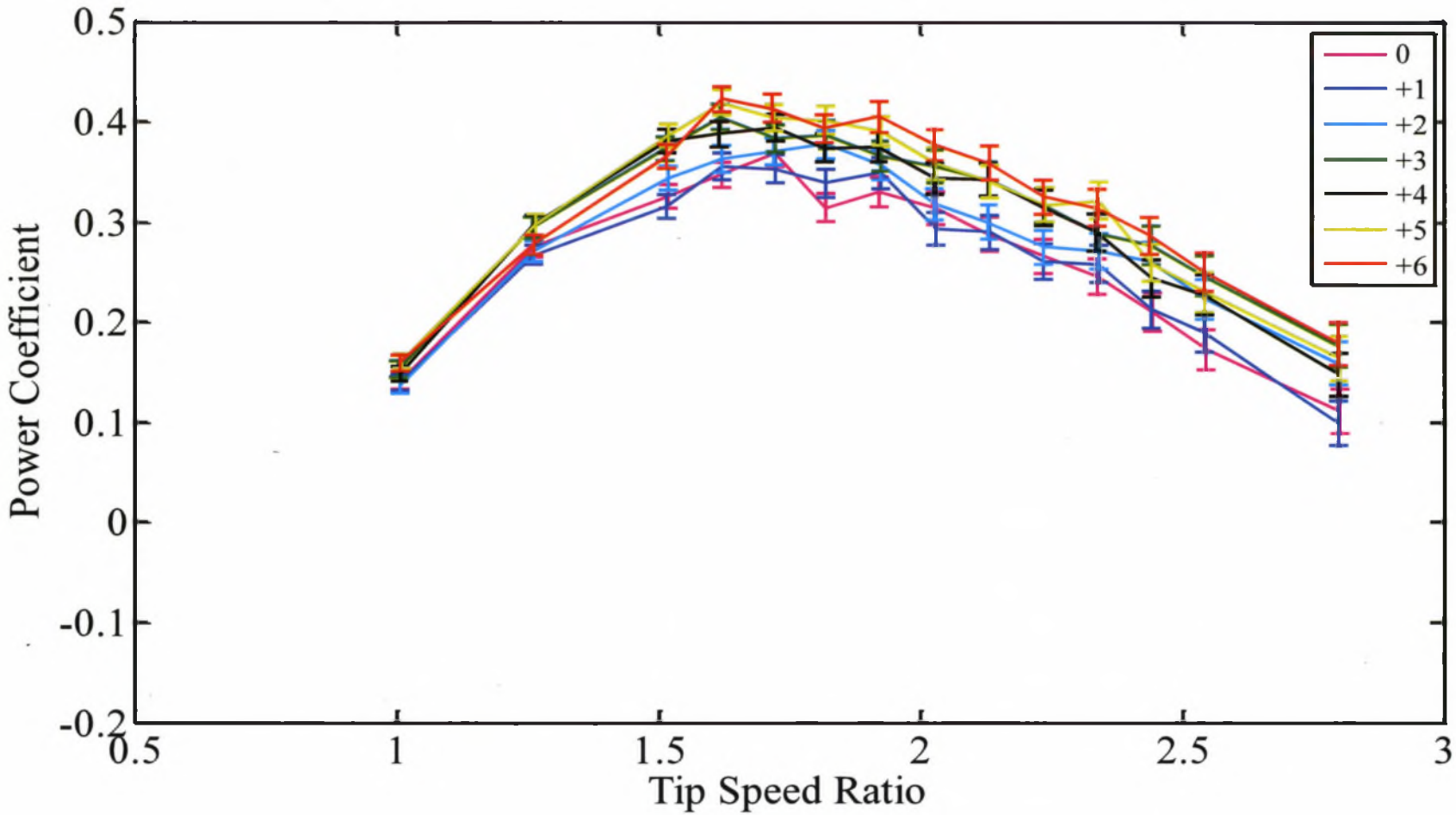

Figure 3.4 – Power coefficient curves for two-blade testing of 3-D printed NACA 0018 blades from toe angles from 0^{o} to $+6^{o}$ with solidity ratio $\sigma = 0.171$ and inflow velocity $U_{\infty} = 0.8$ m/s.

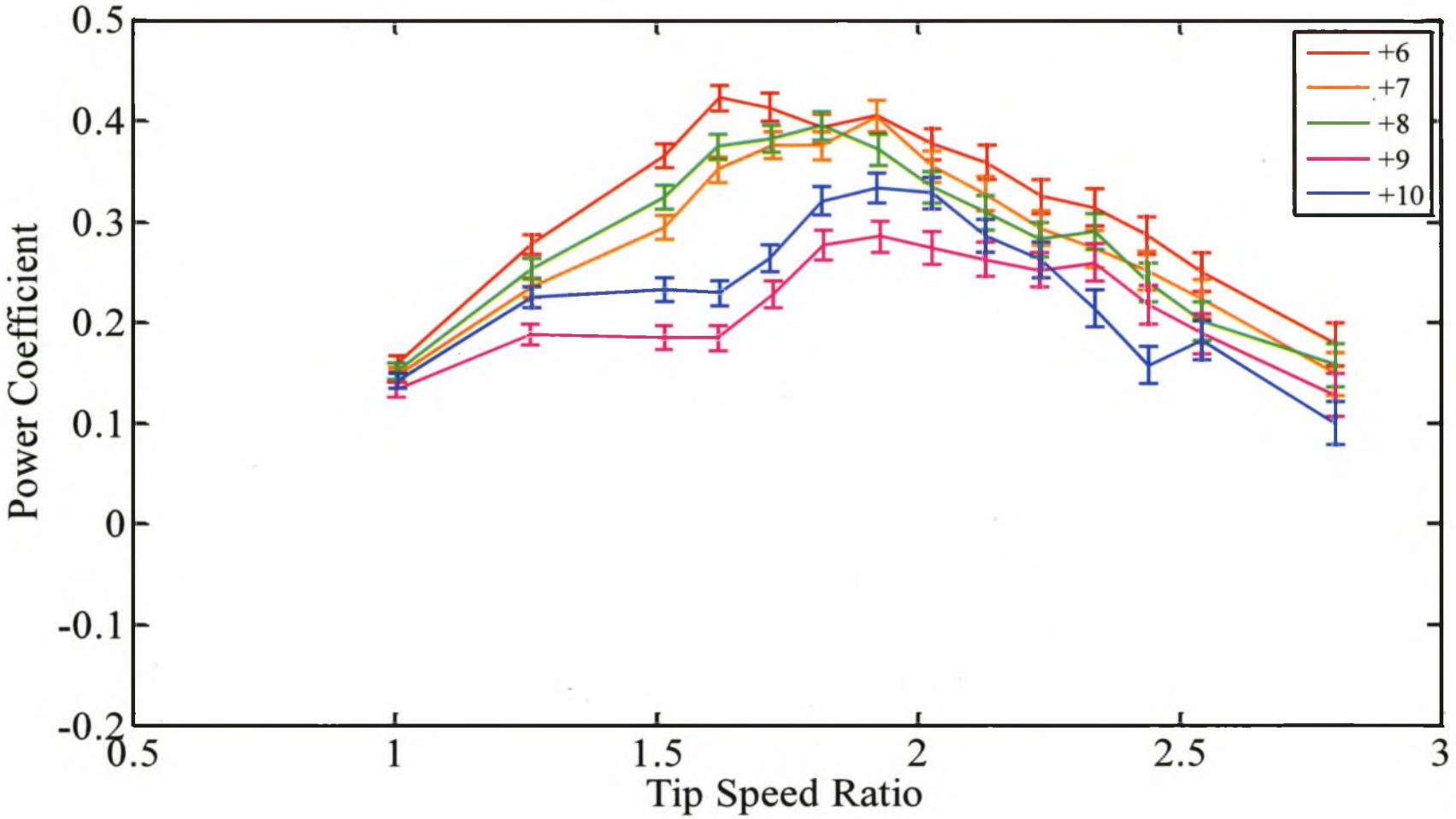

Figure 3.5 – Power coefficient curves for two-blade testing of 3-D printed NACA 0018 blades from toe angles from 0° to +6° with solidity ratio $\sigma = 0.171$ and inflow velocity $U_\infty = 0.8$ m/s.

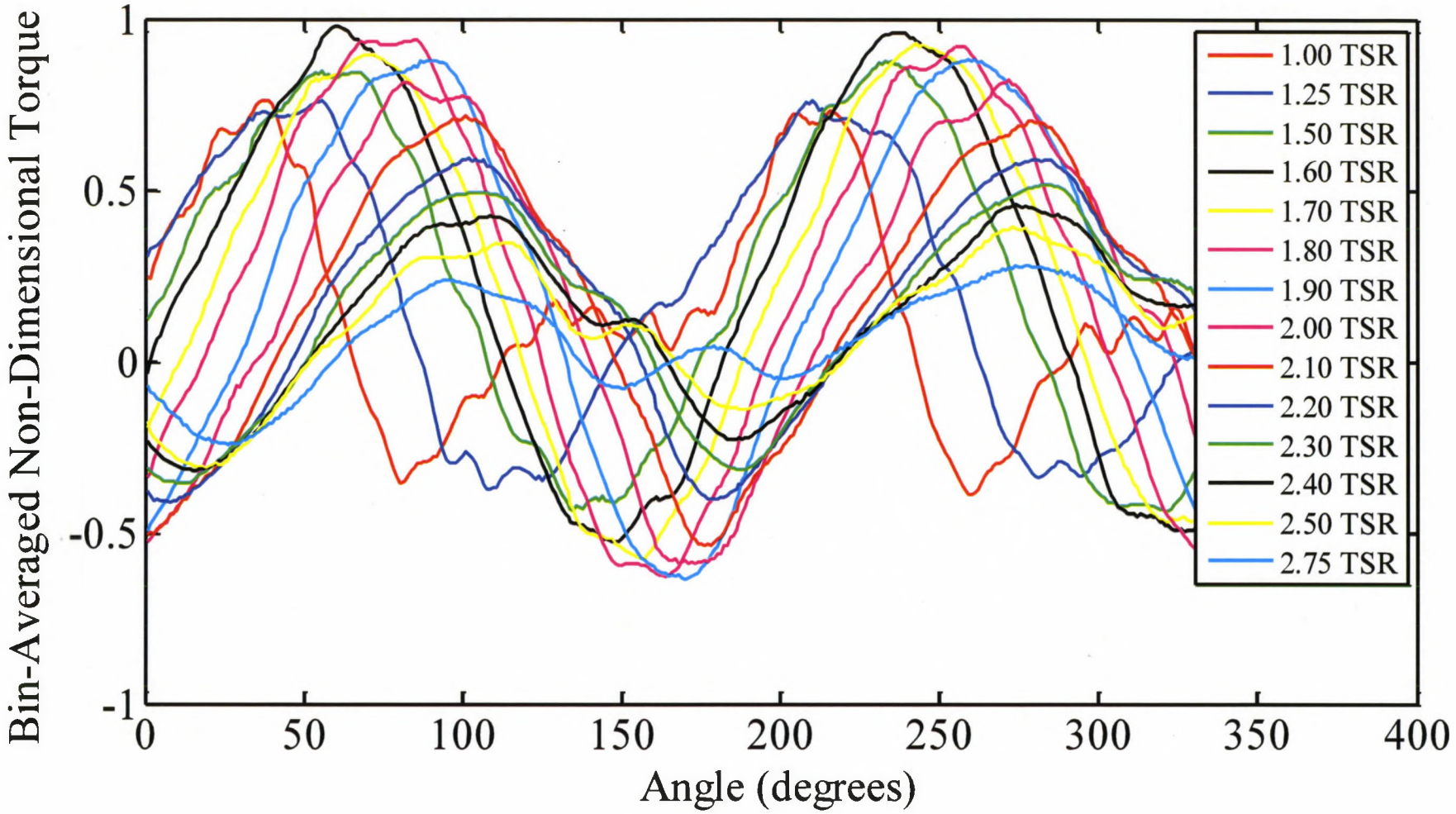

Figure 3.6– Bin-averaged non-dimensional torque curves for two-blade testing of 3-D printed NACA 0018 blades for +6°toe angle with solidity ratio $\sigma = 0.171$ and inflow velocity $U_\infty = 0.8$ m/s.

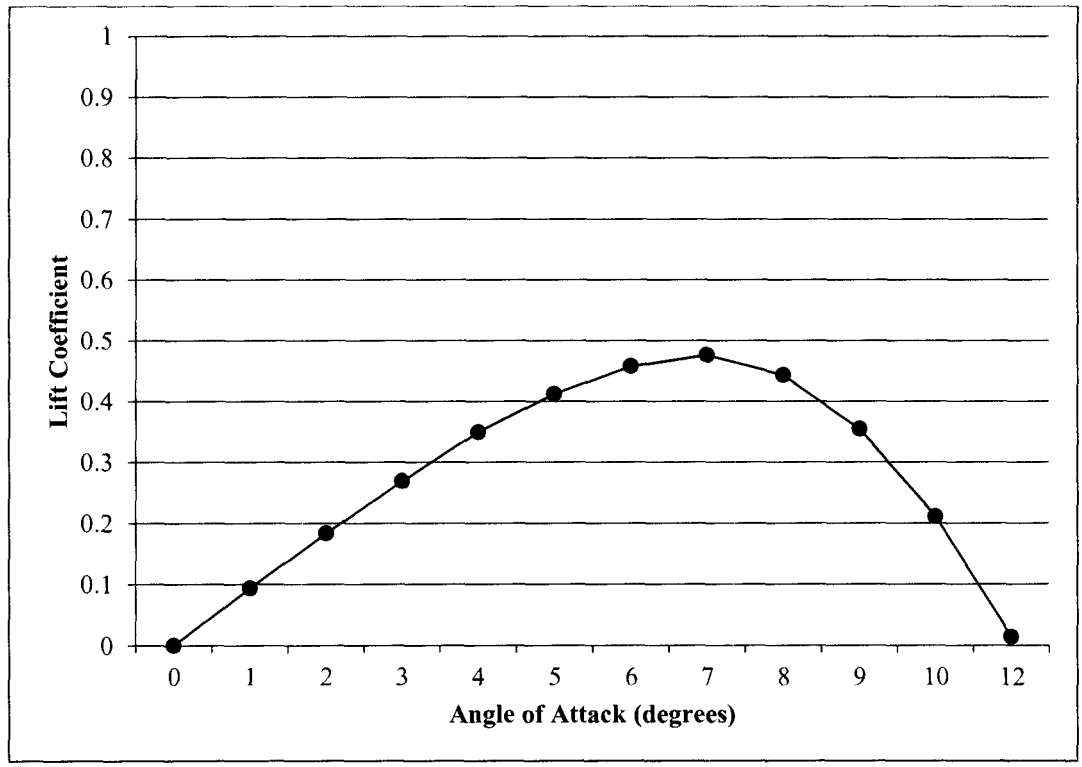

Figure 3.7 – Experimental testing by Sheldahl and Klimas (1981) for NACA 0018 foils showing lift coefficient related to angle of attack.

3.3 Four-Blade Test Results

Four-blade tests were conducted at toe angles from -4^0 to $+10^0$ in increments of one degree. Inflow velocity for all testing was set at 0.8 m/s with the turbine centered in the water column, with a water temperature of 67^0F. With a solidity ratio of 0.343, it was estimated that the max power coefficient would be reached at a TSR between 1 to 1.5, based on experimental solidity data by Shiono et al. (2000). As a result, testing was done at a TSR range from 0.4 to 1.9 to ensure the peak was acquired.

The maximum power coefficient of 23.7% occurred at the $+4^0$ toe angle at a TSR of 1.1 as seen in Fig. 3.7 through 3.10. The $+4^0$ and $+5^0$ toe angles had very similar efficiency curves, varying at peak C_p by 2% and no more than 1.9% in other parts of the curve. The

results show that the efficiency increases steadily from -4^0 toe angle to the peak at $+4^0$. Similarly to the behavior seen in the two-blade results, after maximum lift is reached at $+4^0$, the data becomes less predictable as it decreases from $+5^0$ to $+10^0$.

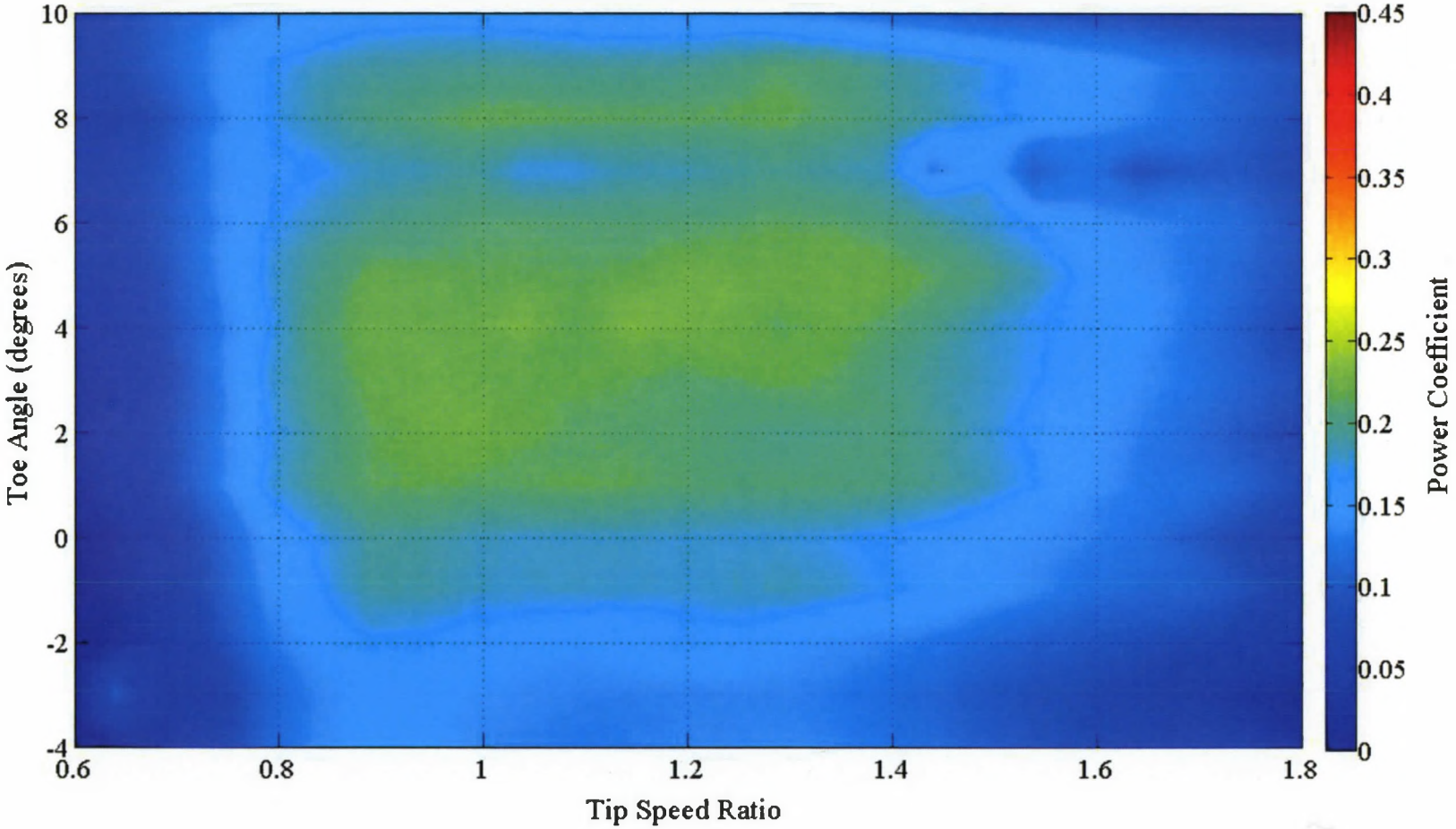

Figure 3.8 – Power coefficient contour plot for four-blade testing of 3-D printed NACA 0018 blades with solidity ratio $\sigma = 0.343$ and inflow velocity $U_\infty = 0.8$ m/s.

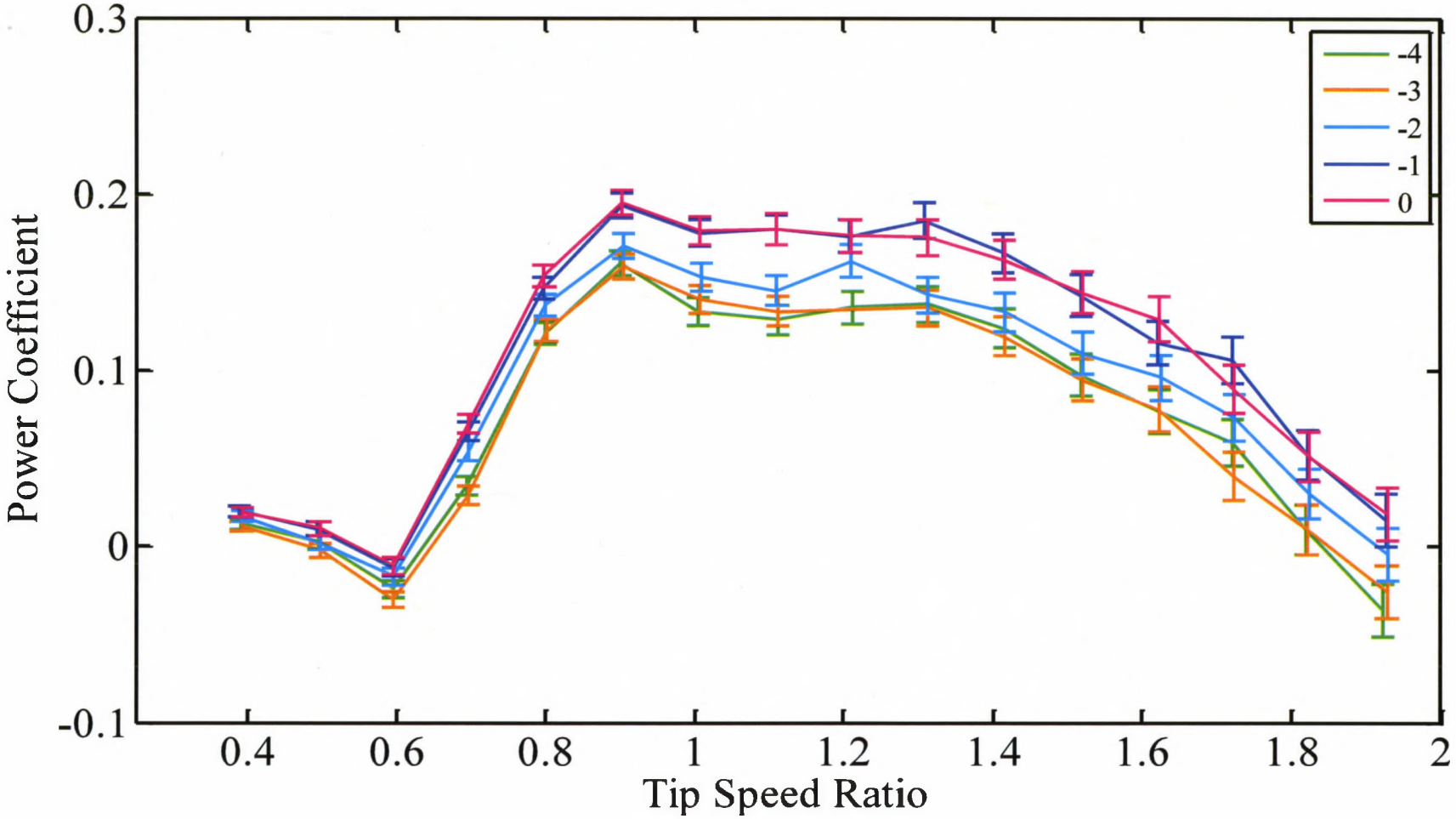

Figure 3.9 – Power coefficient curves for four-blade testing of 3-D printed NACA 0018 blades from toe angles from -4° to 0° with solidity ratio $\sigma = 0.343$ and inflow velocity $U_\infty = 0.8$ m/s.

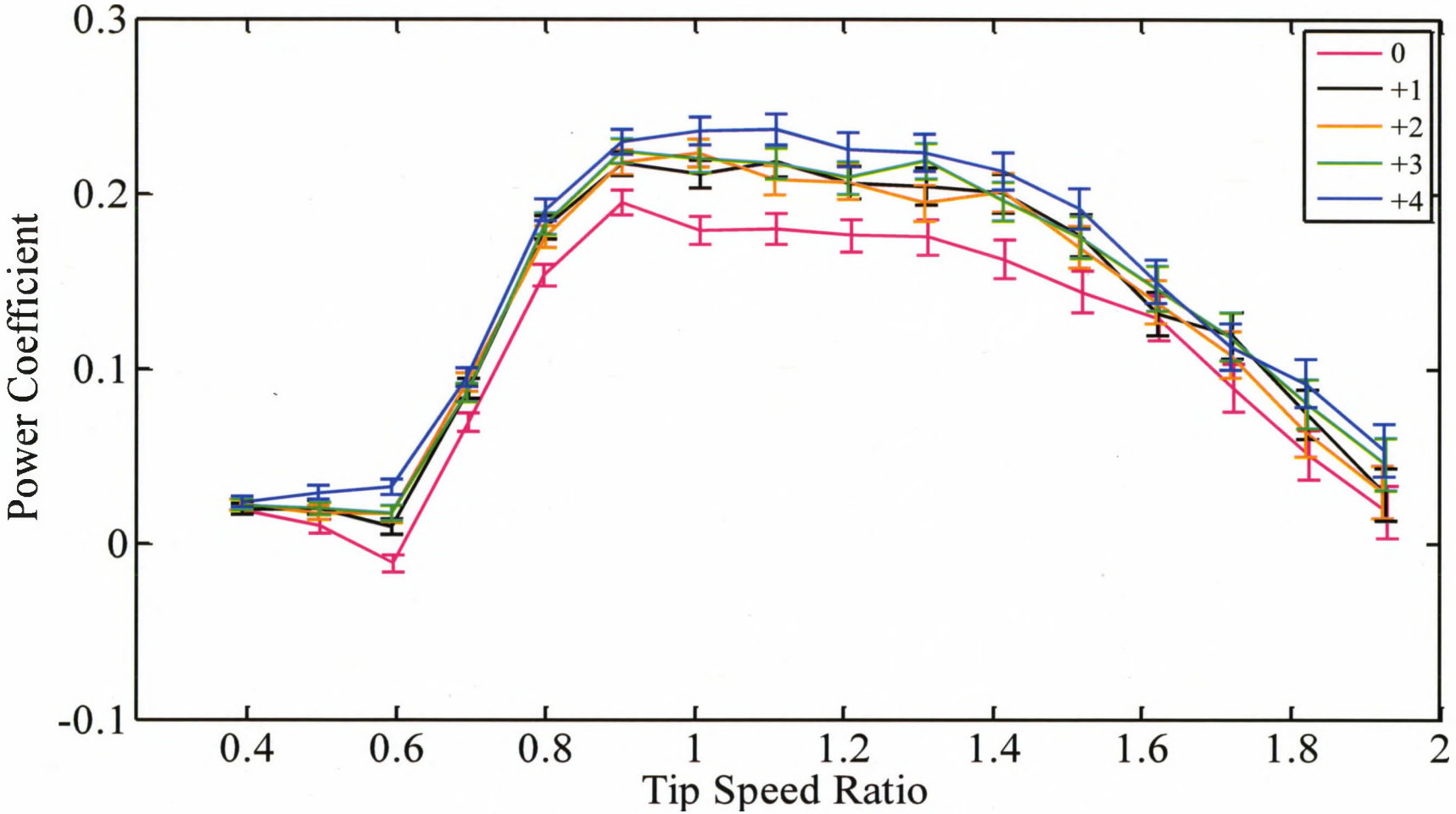

Figure 3.10 – Power coefficient curves for four-blade testing of 3-D printed NACA 0018 blades from toe angles from 0° to +4° with solidity ratio $\sigma = 0.343$ and inflow velocity $U_\infty = 0.8$ m/s.

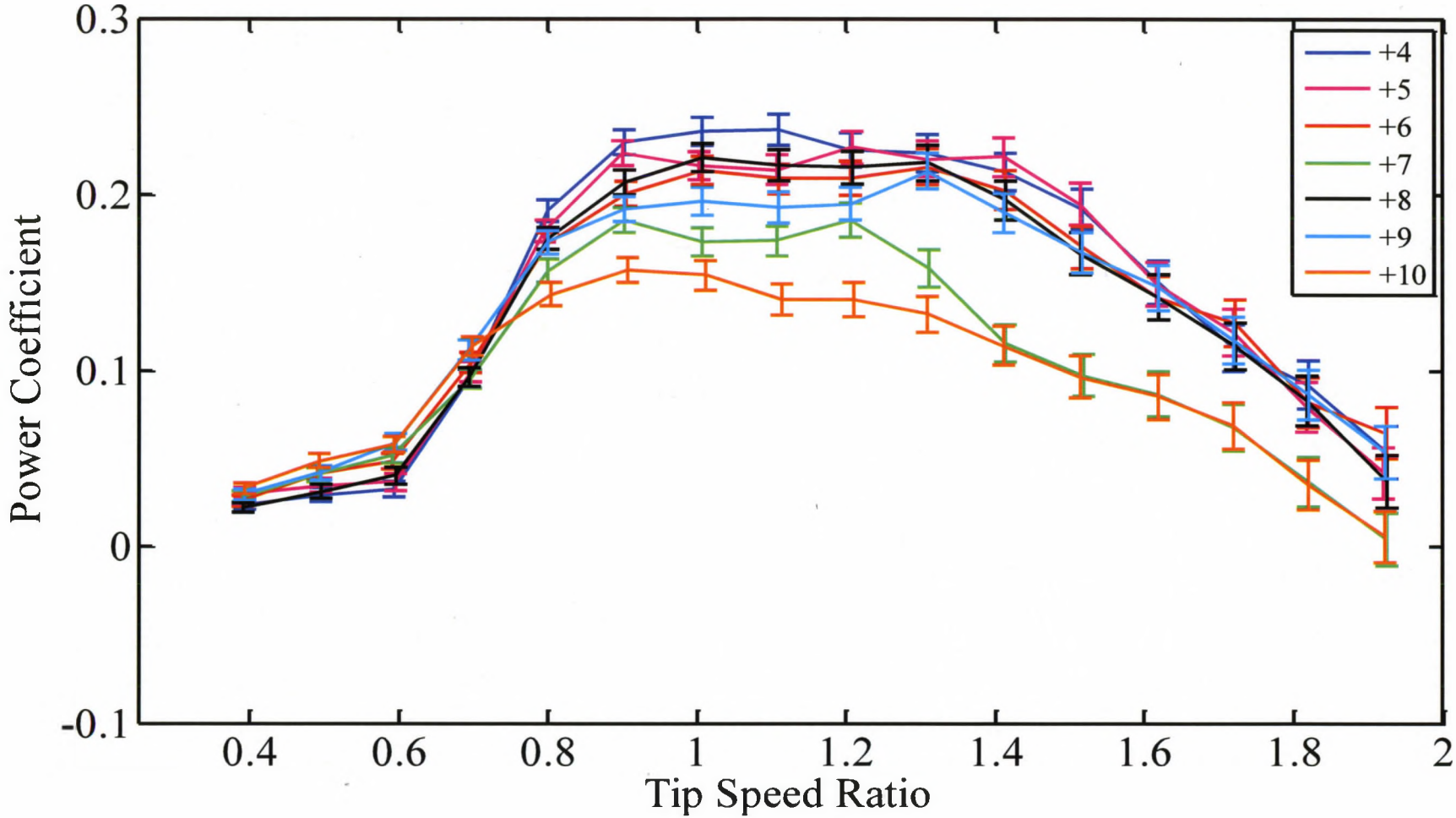

Figure 3.11 – Power coefficient curves for four-blade testing of 3-D printed NACA 0018 blades from toe angles from +4° to +10° with solidity ratio $\sigma = 0.343$ and inflow velocity $U_\infty = 0.8$ m/s.

3.4 Conclusions

As anticipated, the two-blade test results were considerably more efficient than the four-blade tests. At the peak, the two-blade turbine was better by a difference of 18.7%. The plots hold a very similar shape between the two different setups, but with a substantial shift in the data. As seen in Fig. 3.11, the two-blade curve passes directly through the four-blade curve around a TSR of 1.1 where the four-blade data peaks. Testing by Shiono et al. (2000) shows this same shift and intersection of data at similar solidities. The results show that although the two-blade turbine is more efficient, it must be operated at higher TSR to achieve peak efficiency; however, this is still a much lower TSR than other axial designs.

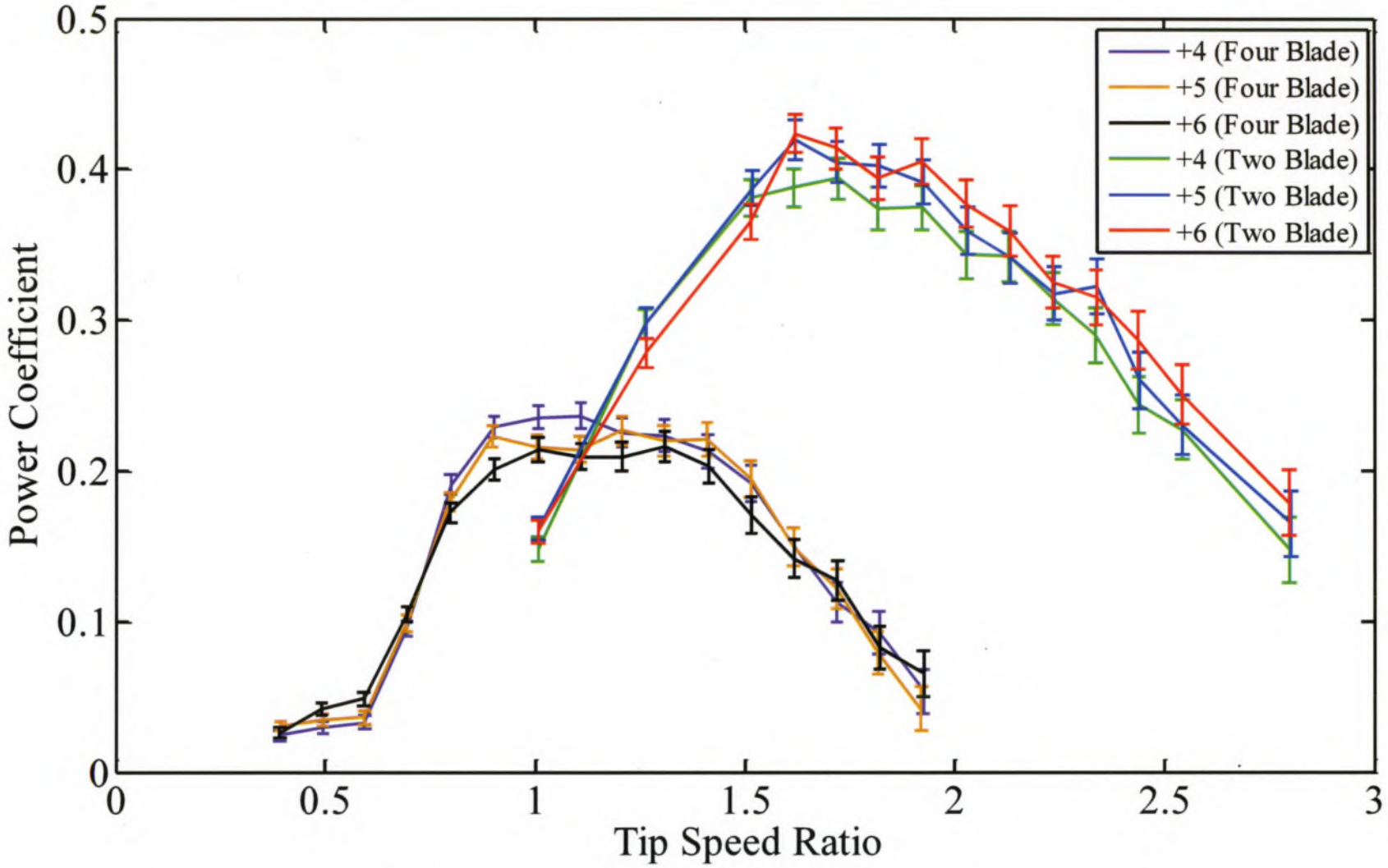

Figure 3.12 – Power coefficient curve comparison for two-blade and four-blade testing of NACA 0018 blades from toe angles from +4° to +6° and inflow velocity U_∞ = 0.8 m/s.

CHAPTER 4

CAMBERED FOIL RESULTS

The cambered NACA 4418 foils were tested in the two-blade configuration at multiple toe angles. Power coefficient curves were compared for each setup to find the peak efficiency and optimal toe angle. The goal of this test set was to determine if cambered foils were more efficient than symmetrical and reverse camber foils, which will be discussed in the following chapter.

4.1 Geometry of NACA 4418 Blades

The cambered profile of the NACA 4418 blade is shown in Fig. 4.1. The blades used in the testing had a 3.5 inch chord length, identical to the symmetrical NACA 0018. The NACA 4418 foil is extremely similar to the NACA 0018, having the same thickness but adding a slight camber at 4% of the total chord length. This blade was chosen because of its strong similarities with the NACA 0018 it is compared against.

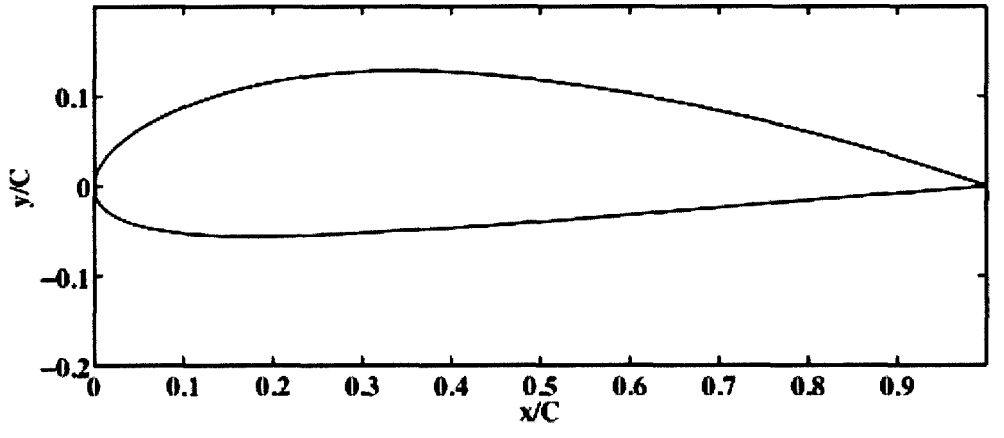

Figure 4.1 – Profile view of the symmetrical NACA 4418 blade

4.2 Two-Blade Test Results

Two-blade tests were executed at toe angles spanning from -4^0 to 0^0 in two degree increments, from $+3^0$ to $+7^0$ in one degree increments, and one test was taken at $+10^0$. Inflow velocity was set at 0.8 m/s for all testing with the turbine centered in the water column. With an identical chord length as the NACA 0018 foils, this setup possessed a solidity ratio of 0.171. Again, based on the solidity data by Shiono et al. (2000), the TSR range was set from 1 to 3 in order to capture the peak expected to be between a TSR of 1.6 and 2.

This test set was taken during the winter months when the water temperature was 48^0F, a difference of 19^0F less than summer test conditions. As a result of the temperature drop, the viscosity and density increased, which directly affects the efficiency of the turbine (see Appendix C). To provide comparable data with the NACA 4418 cambered and reverse cambered foils, the two-blade symmetrical NACA 0018 foils were tested again at the 48^0F water temperature for the study in this chapter. The peak power coefficient occurred at a $+6^0$ toe angle at a TSR of 1.6. The maximum power coefficient was 37.5%, which can be seen in Fig. 4.2 to 4.5.

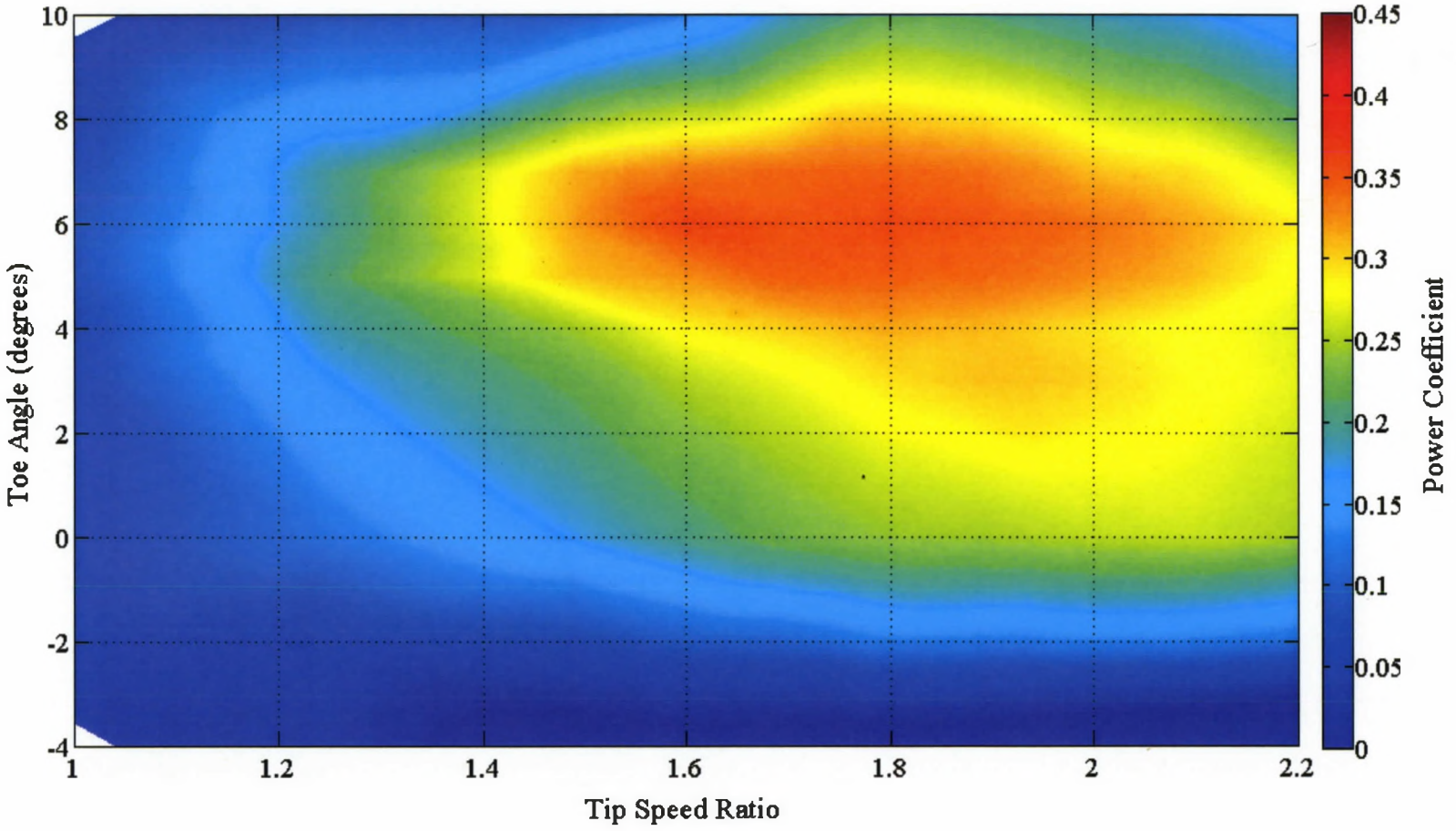

Figure 4.2 – Power coefficient contour plot for two-blade testing of 3-D printed NACA 4418 blades with solidity ratio $\sigma = 0.171$ and inflow velocity $U_\infty = 0.8$ m/s.

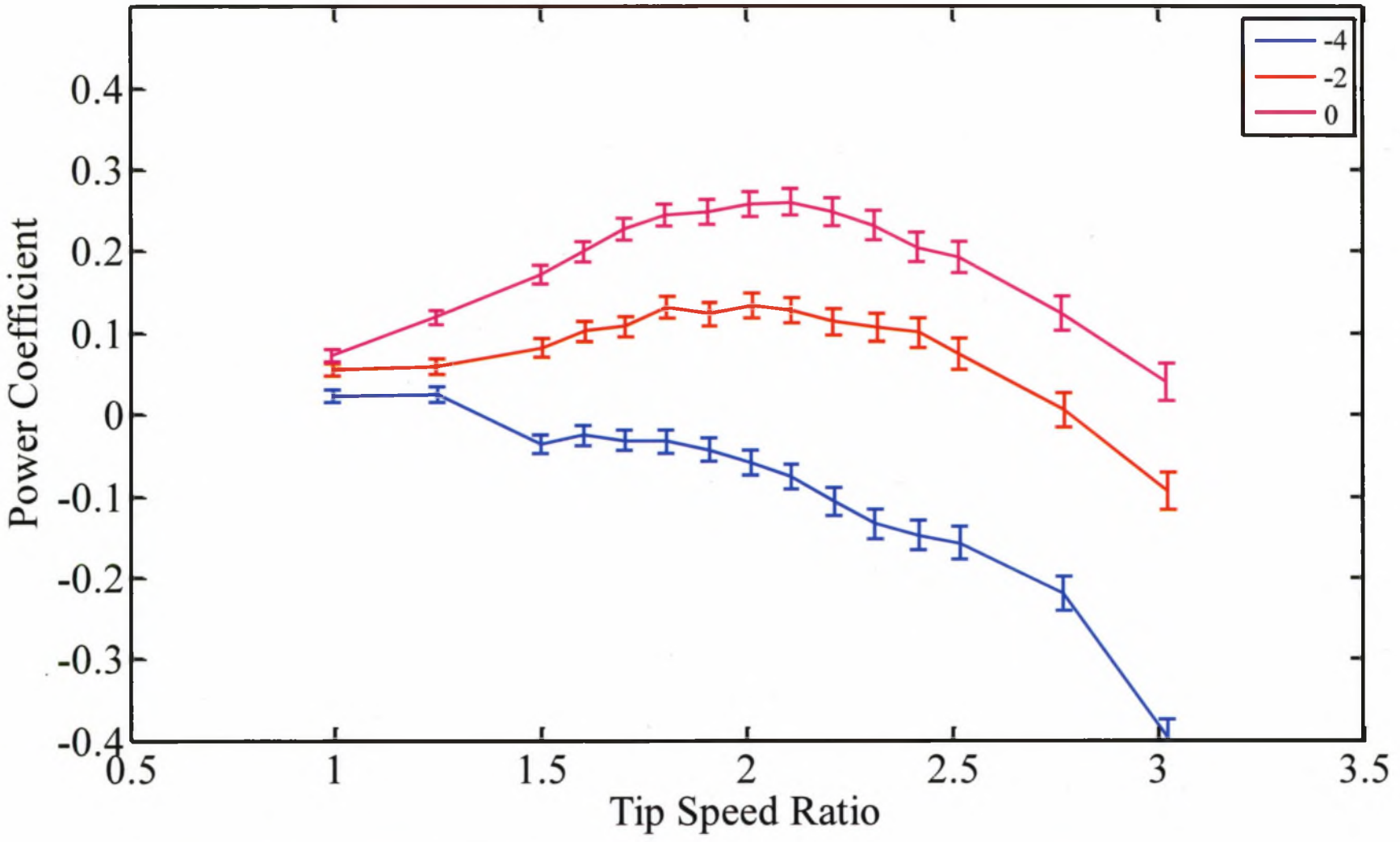

Figure 4.3 – Power coefficient curves for two-blade testing of 3-D printed NACA 4418 blades from toe angles from -4° to 0° with solidity ratio $\sigma = 0.171$ and inflow velocity $U_\infty = 0.8$ m/s.

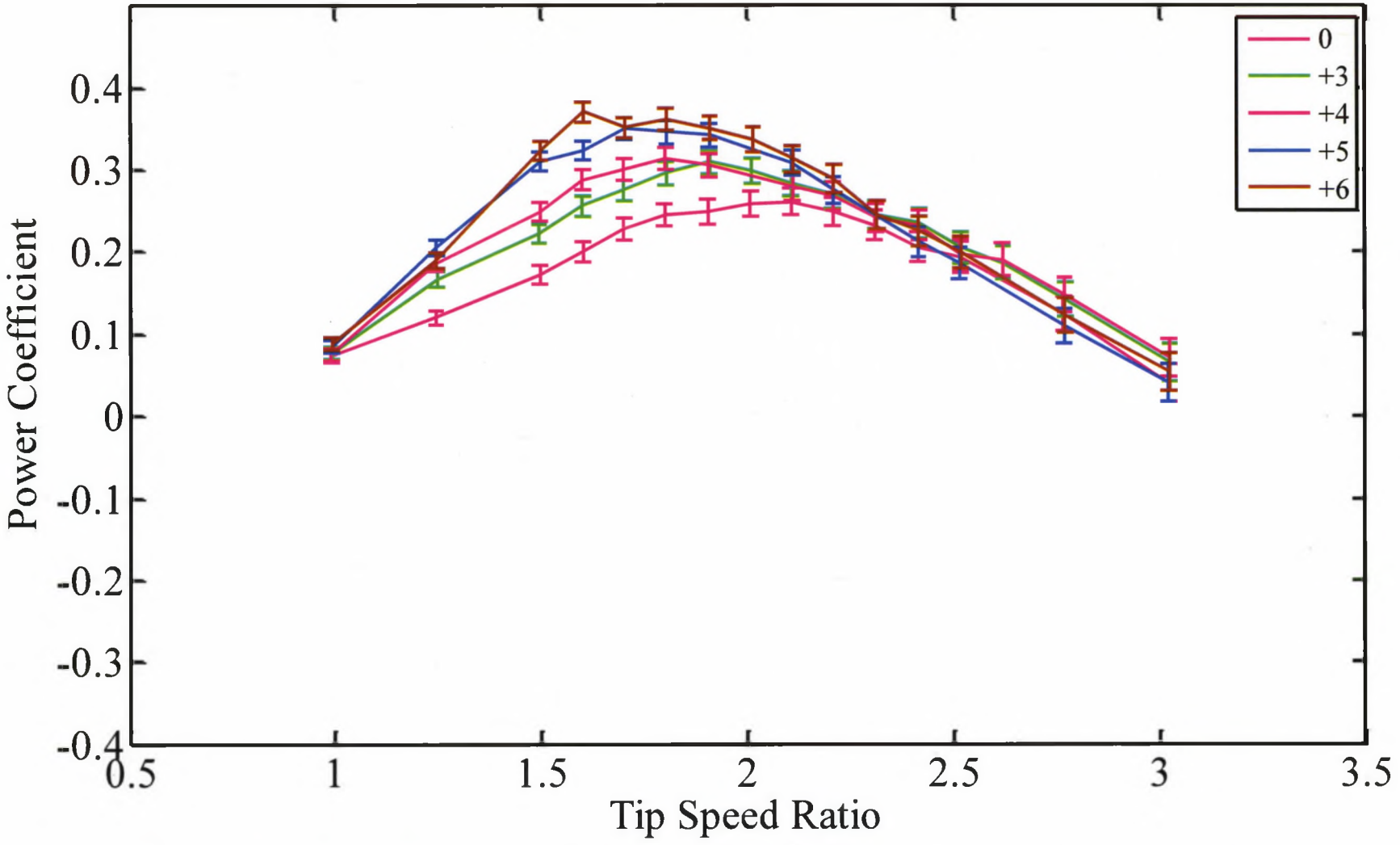

Figure 4.4 – Power coefficient curves for two-blade testing of 3-D printed NACA 4418 blades from toe angles from 0^{o} to $+6^{o}$ with solidity ratio $\sigma = 0.171$ and inflow velocity $U_{\infty} = 0.8$ m/s.

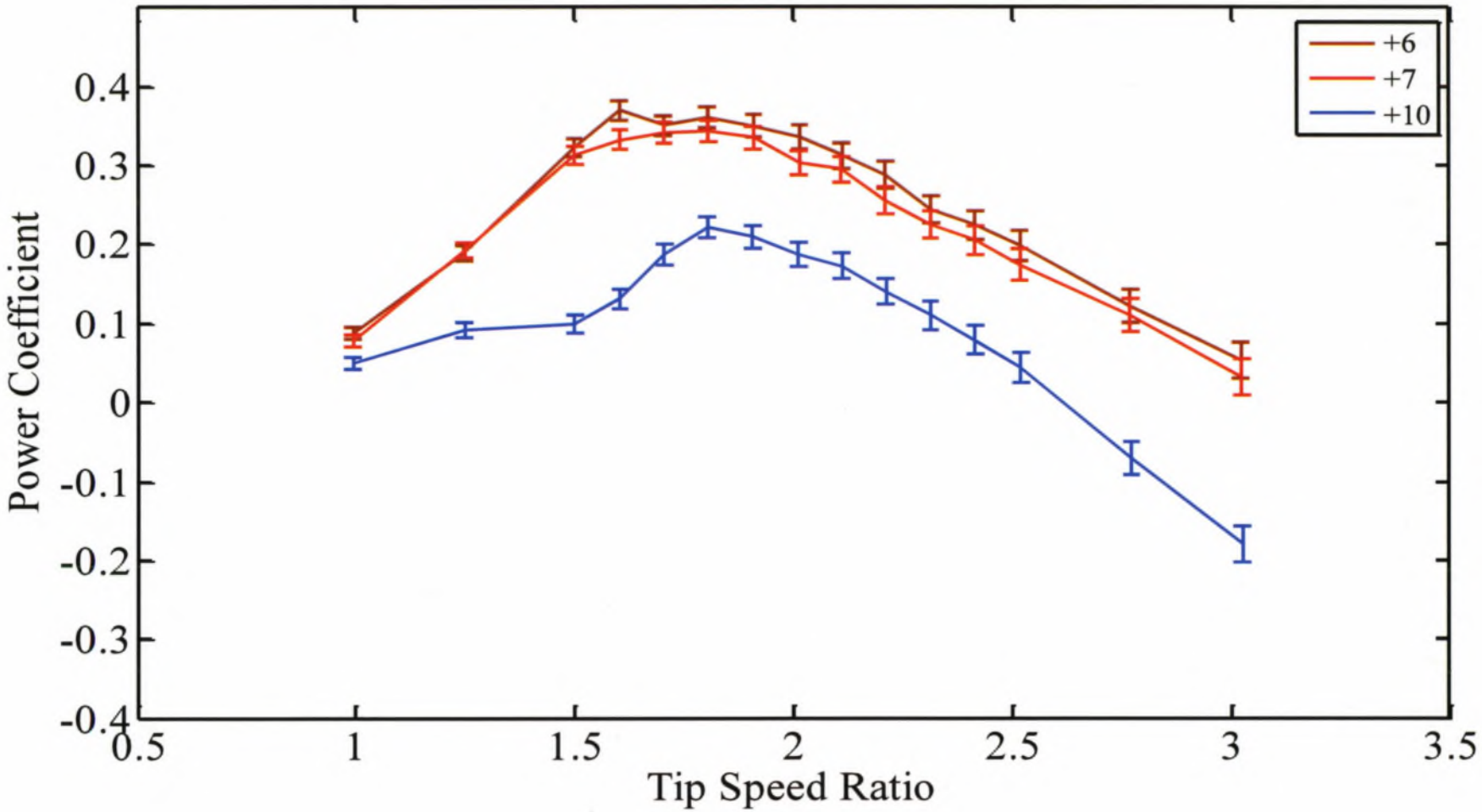

Figure 4.5 – Power coefficient curves for two-blade testing of 3-D printed NACA 4418 blades from toe angles from +6° to +10° with solidity ratio $\sigma = 0.171$ and inflow velocity $U_\infty = 0.8$ m/s.

4.3 Comparison to Symmetrical Foils

Although the addition of camber can significantly change lift and drag characteristics in certain cases (Abbott and von Donhoeff, 1959), for these selected foils it does not improve the turbine performance in this study and actually results in a decrease in efficiency. With the NACA 0018 foils reaching a maximum power coefficient of 41.2% and the NACA 4418 peaking at 37.5%, the symmetrical foils are more efficient by a difference of 3.7%. Over the span of the curves the difference between efficiencies at corresponding tip speed ratios is substantial, showing the NACA 0018 foils to be over 5% more efficient at most tip speed ratios and reaching almost 8% at some points.

As mentioned before, this study was conducted during the winter months when the water temperature was approximately 20^0F cooler than the summer tests. It is important to note that not only were the cambered foils not as efficient as the symmetrical foils in winter testing, but both were less efficient than the results from symmetrical testing during the summer. This is most likely from the viscosity change due to the large drop in temperature. Comparison of winter and summer data for the symmetrical NACA 0018 blades can be found in Appendix C.

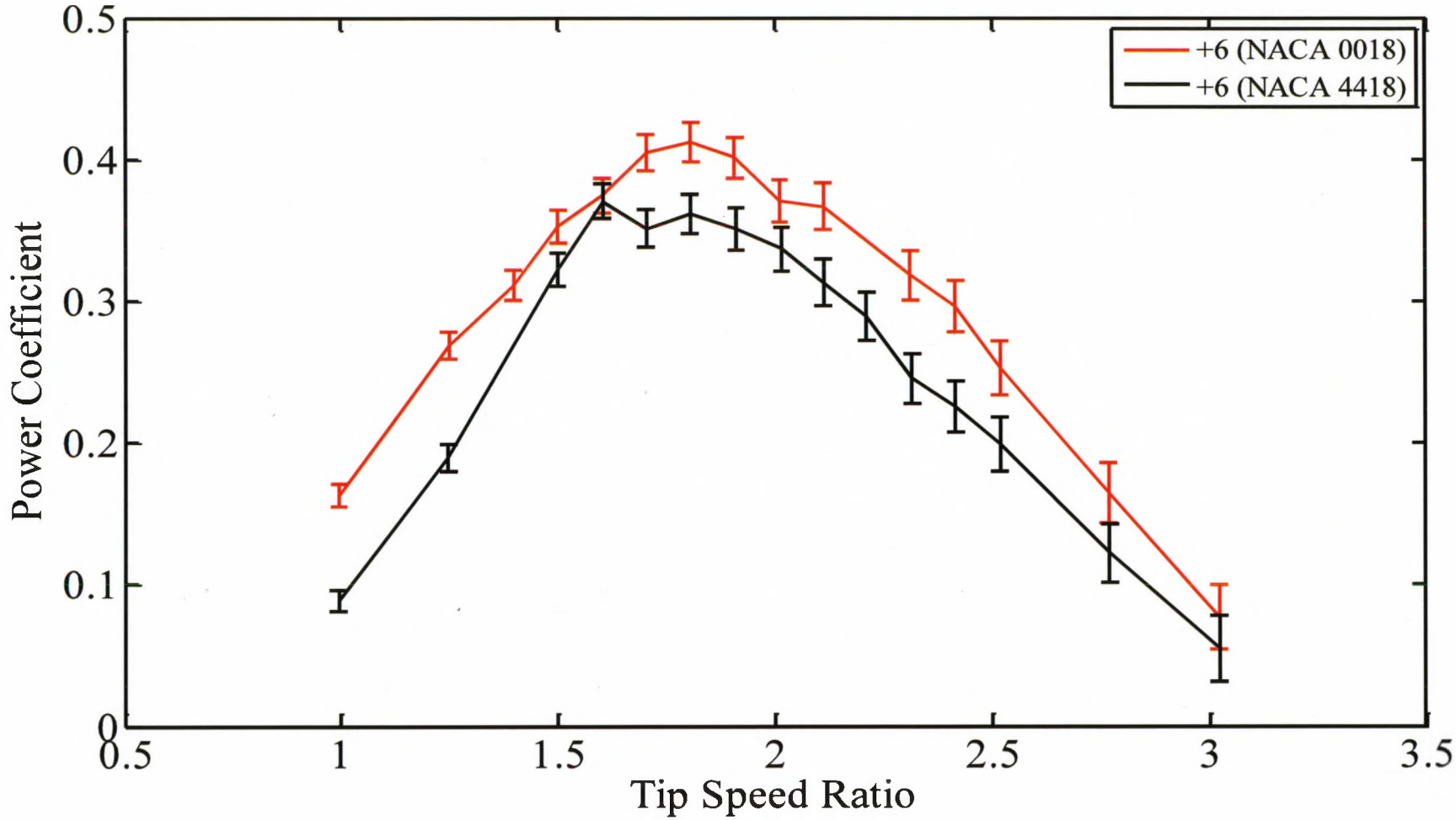

Figure 4.6 – Power coefficient comparison curves for two-blade testing of 3-D printed NACA 4418 blades and NACA 0018 blades. The peak power coefficient occurred at $+6^0$ toe angle. Solidity ratio $\sigma = 0.171$ and inflow velocity $U_\infty = 0.8$ m/s.

CHAPTER 5

REVERSE CAMBER FOIL RESULTS

The cambered NACA 4418 foils were tested again, but in the reverse cambered configuration. Since lower solidity had proven to be more efficient, this set of tests was done only with the two-blade setup. For each setup, power coefficient curves were compared to determine the peak efficiency and optimal toe angle and TSR. This set of tests was compared to both the symmetrical NACA 0018 foils as well as the cambered NACA 4418 in the typical configuration with the concave side facing inward toward the center of the turbine.

5.1 Geometry of Reverse Camber NACA 4418 Blades

The cambered profile of the NACA 4418 blade in the reverse orientation can be seen in figure 5.1. Again, there is a 4% camber over the total chord length and the same thickness as the symmetrical NACA 0018 foils.

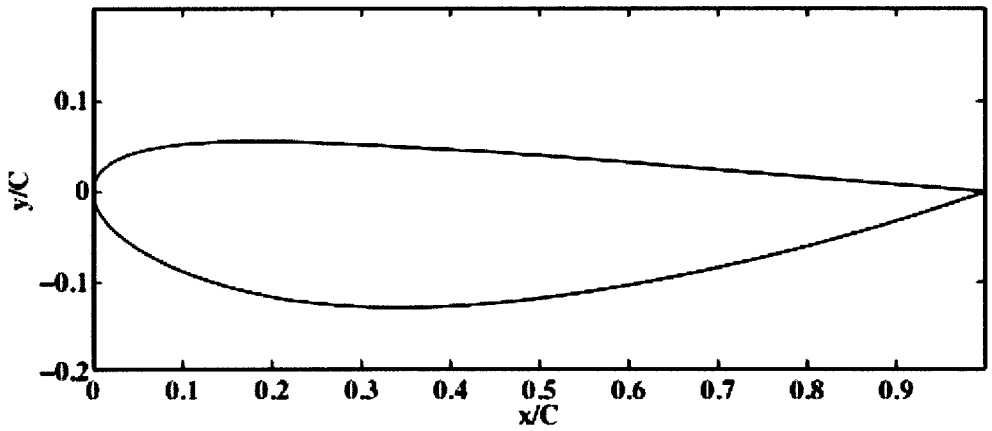

Figure 5.1 – Profile view of the reverse camber NACA 4418 blade

5.2 Two-Blade Test Results

Two-blade tests were executed at toe angles spanning from 2^0 to 10^0 in one degree increments and one test was taken at 0^0. Inflow velocity was set at 0.8 m/s for all testing with the turbine centered in the water column. This test set was taken at a water temperature of 48^0F. With an identical chord length as the NACA 4418 foils, this setup had a solidity ratio of 0.171. Again, based on the solidity data by Shiono et al. (2000), the peak efficiency was expected to occur around a TSR of 1.6 to 2. Initially, the TSR range was set to run from 1 to 2.75, but after a few preliminary tests the range was changed to a range of 0.6 to 2.4 to ensure an accurate representation of the curve was captured.

This test set was the least efficient compared to the symmetrical NACA 0018 and regular cambered NACA 4418 foils. The peak power coefficient was 35.1% at a toe angle of $+4^0$ and TSR of 1.7. Test set results are shown in Fig. 5.2 to 5.5.

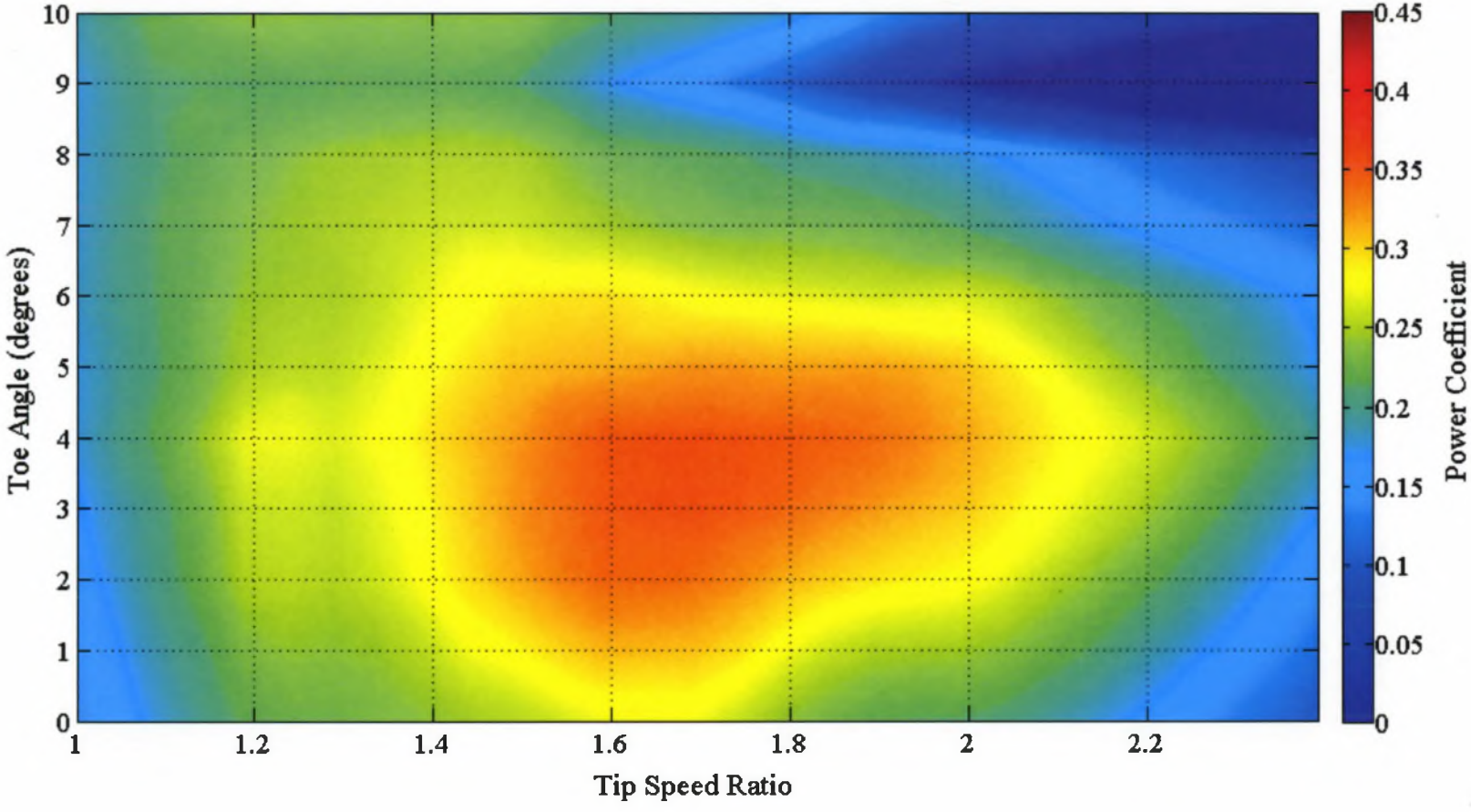

Figure 5.2 – Power coefficient contour plot for two-blade testing of reverse camber 3-D printed NACA 4418 blades with solidity ratio $\sigma = 0.171$ and inflow velocity $U_\infty = 0.8$ m/s.

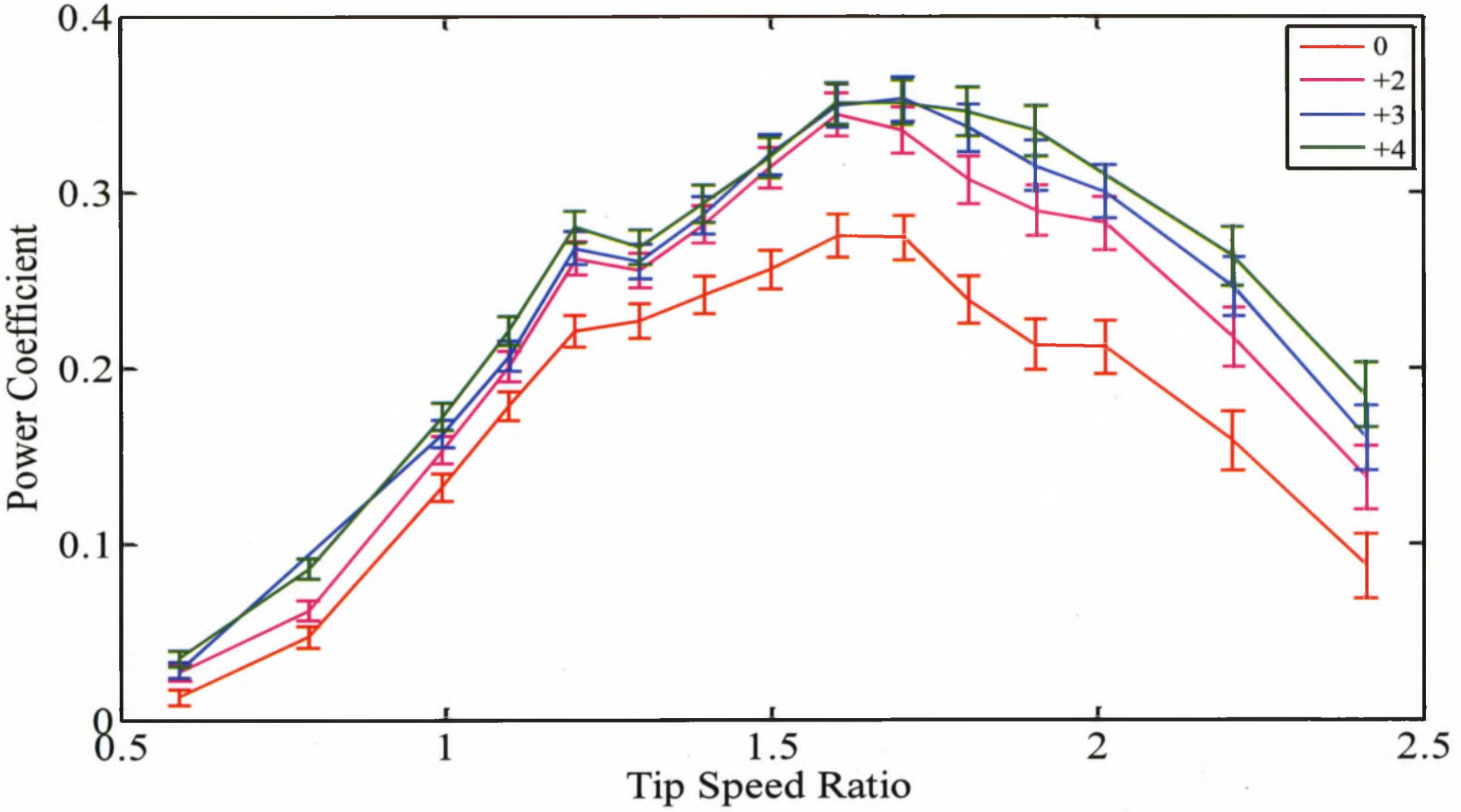

Figure 5.3 – Power coefficient curves for two-blade testing of reverse camber 3-D printed NACA 4418 blades from toe angles from 0° to +4° with solidity ratio $\sigma = 0.171$ and inflow velocity $U_\infty = 0.8$ m/s.

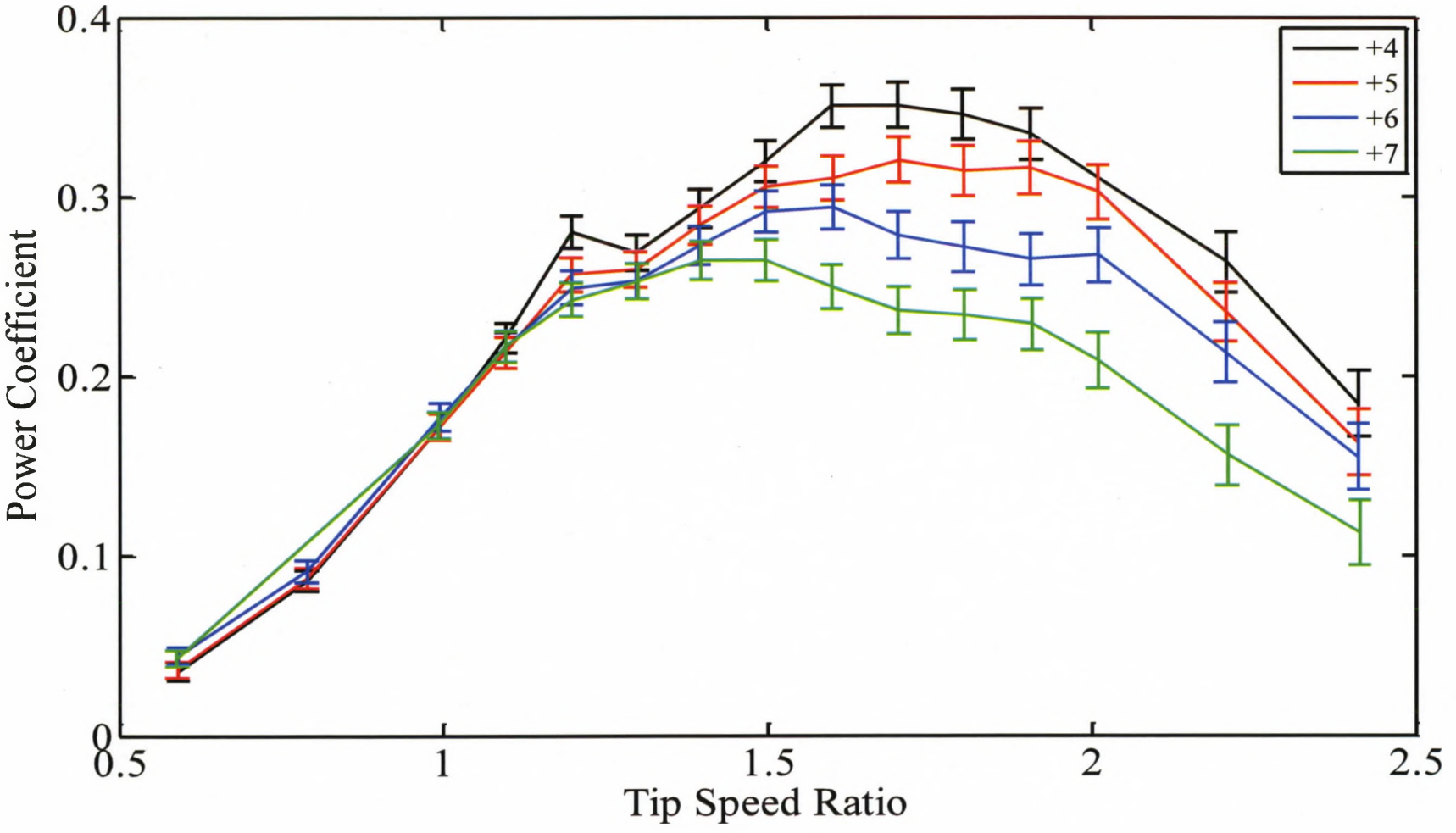

Figure 5.4 – Power coefficient curves for two-blade testing of reverse camber 3-D printed NACA 4418 blades from toe angles from +4° to +7° with solidity ratio $\sigma = 0.171$ and inflow velocity $U_\infty = 0.8$ m/s.

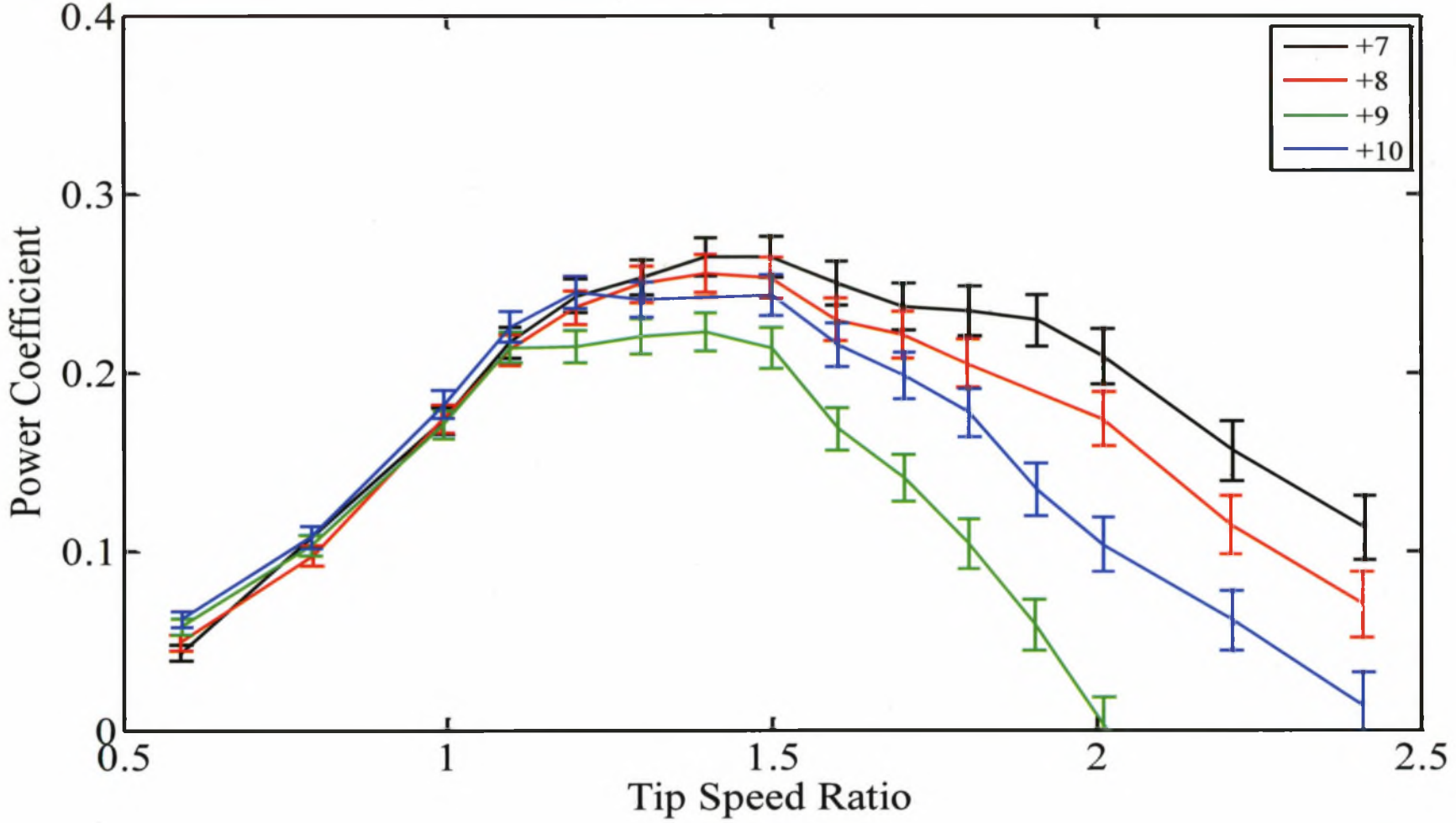

Figure 5.5 – Power coefficient curves for two-blade testing of reverse camber 3-D printed NACA 4418 blades from toe angles from +7° to +10° with solidity ratio $\sigma = 0.171$ and inflow velocity $U_\infty = 0.8$ m/s.

5.3 Comparison to Symmetric and Regular Camber Foils

The results of the reverse camber NACA 4418 foils proved to be less efficient than both the symmetrical NACA 0018 foils and the regular camber NACA 4418 foils. The comparison of the peak power coefficient curves for all three blades in Fig 5.6 shows the difference between the three profiles. At the peak of each curve, the regular camber NACA 4418 blades were more efficient by 2.4% and the symmetrical NACA 0018 blades were more efficient by 6.1%.

It is important to note that the reverse camber NACA 4418 blades reached maximum performance at a lower toe angle than the regular camber NACA 4418 and the symmetrical 0018 foils. This may be due to the fact that the reverse camber foils stall much more quickly than the symmetrical and regular camber foils, with the zero lift line at 5 degrees for the NACA 4418 foils and 0 degrees for the NACA 0018 foils. When comparing all three profiles at a $+6^0$ toe angle, as in Fig. 5.7, the performance difference became even more apparent. At this angle, the reverse camber blades were less efficient than the regular camber blades and symmetrical blades by 8.1% and 11.8%, respectively. The reverse camber NACA 4418 foils did show higher efficiencies than the other two profiles at some of the lower TSRs. At the $+4^0$ toe angle the reverse camber foils were more efficient than the regular camber foils by almost 9% at a TSR of 1, however, once the reverse cambered blades reached stall the performance dropped off rapidly.

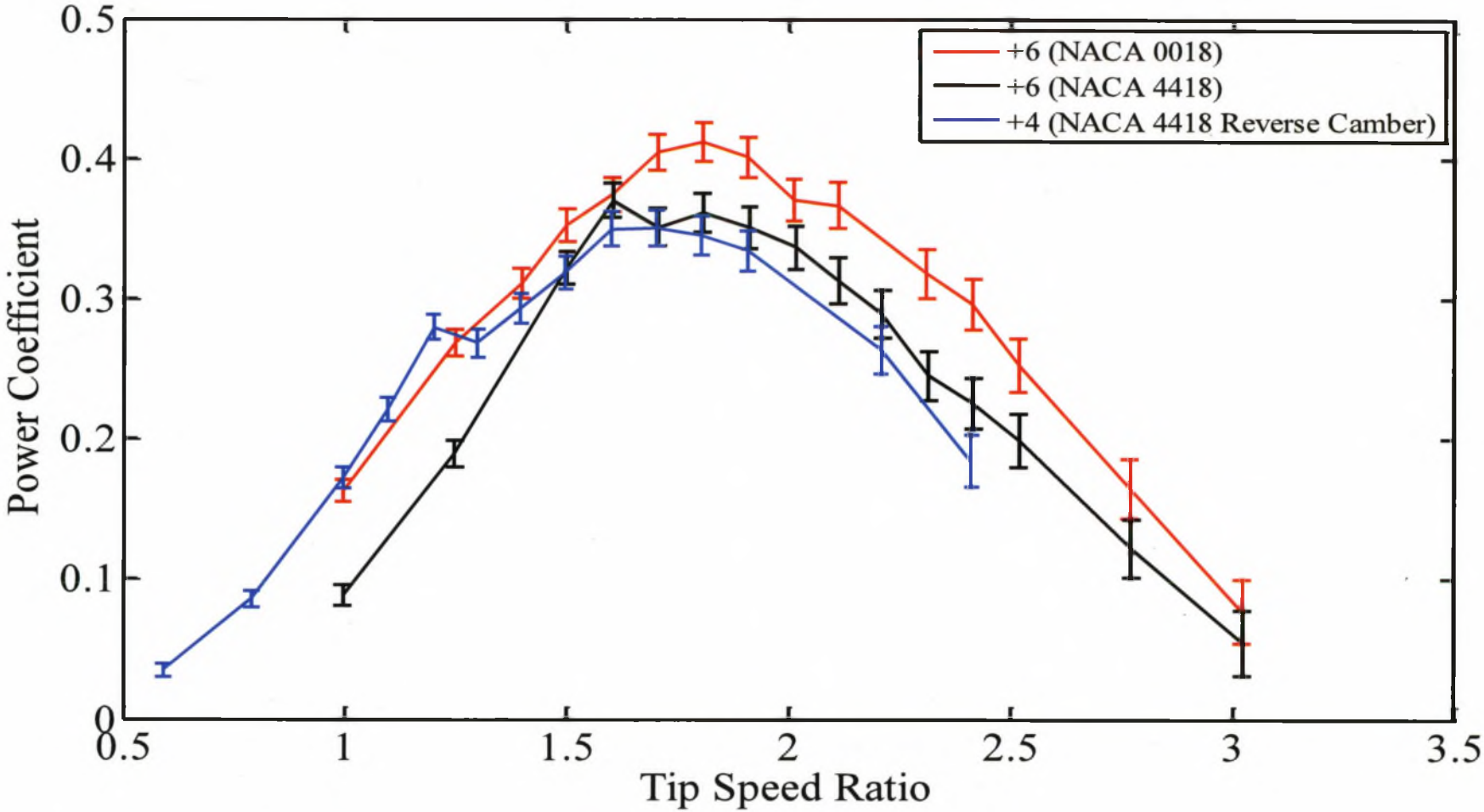

Figure 5.6 – Comparison of peak power coefficient curves for two-blade testing of 3-D printed NACA 0018 blades, NACA 4418 blades, and reverse camber NACA 4418 blades. Curves are from toe angles that showed best performance for each profile. Each profile was tested with solidity ratio $\sigma = 0.171$ and inflow velocity $U_\infty = 0.8$ m/s.

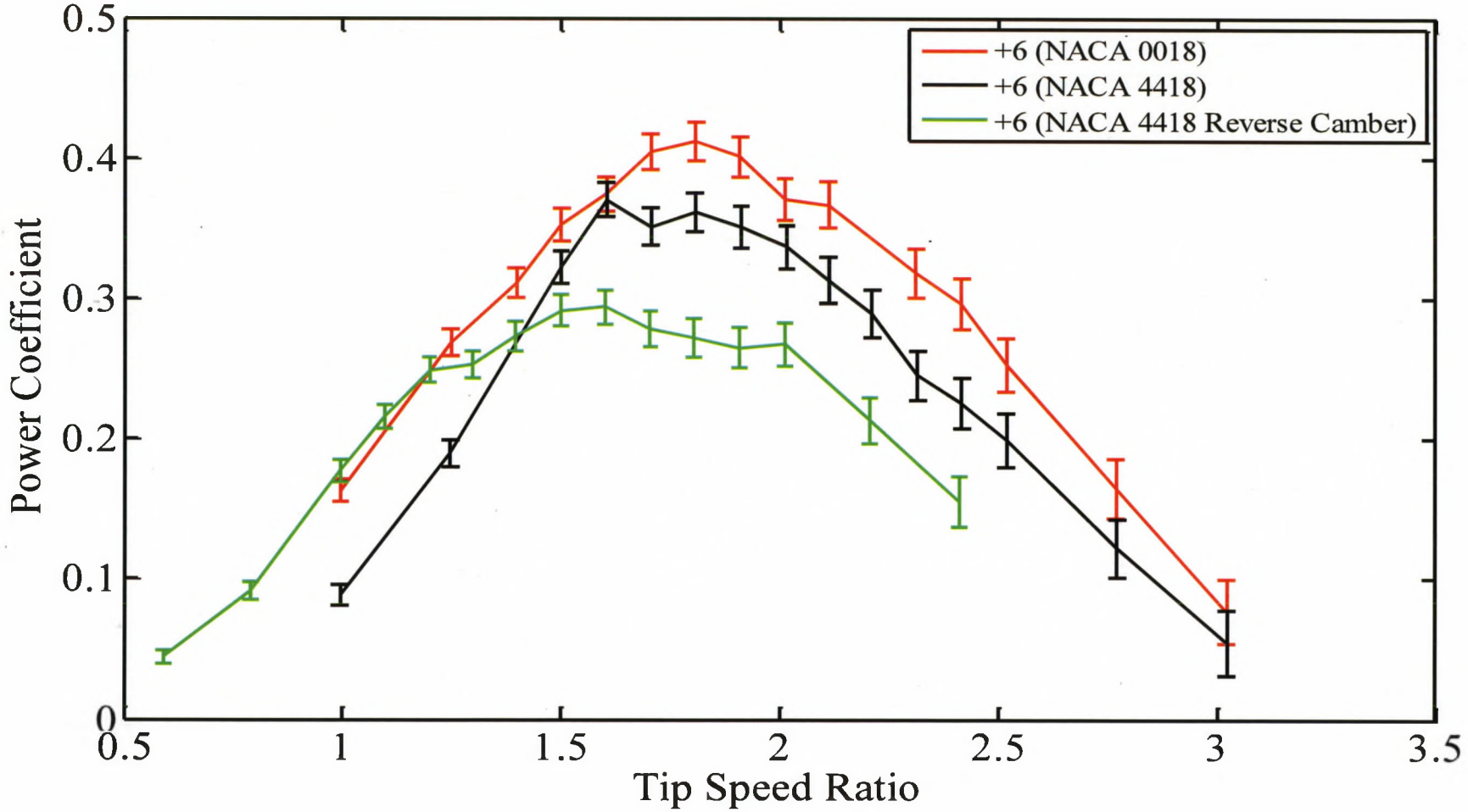

Figure 5.7 – Comparison of power coefficient curves for two-blade testing of 3-D printed NACA 0018 blades, NACA 4418 blades, and reverse camber NACA 4418 blades at $+6^0$ toe angle. Each profile was tested with solidity ratio σ = 0.171 and inflow velocity U_∞ = 0.8 m/s.

5.4 Conclusions

As anticipated, the two-blade symmetrical NACA 0018 foils were the most efficient out of all three blade profiles. The reverse camber NACA 4418 blades could be an option for systems operating at very low TSR, but the power coefficient would be less than half of the maximum performance of the symmetrical NACA 0018 foils.

Kerwin (2001) suggests that an ideal camber line would produce a constant pressure over the chord length to produce fixed lift with minimum reduction in local pressure. In this case, the camber in this study may need to be adjusted slightly to distribute the load evenly along the chord length and ensure circulation decreases to the trailing edge to avoid adverse pressure gradients and boundary layer separation.

REFERENCES

Adamski, S., 2013, "Numerical Modeling of the Effects of a Free Surface on the Operating Characteristics of Marine Hydrokinetic Turbines," University of Washington.

Bertin, J.J., and Smith, M. L., 1979, "Aerodynamics for Engineers," Prentice-Hall, Englewood Cliffs, NJ.

Cameron, M., 2013. Personal communication.

Charlier, R. H., 1982, "Tidal Energy," Van Nostrand Reinhold Company, New York, NY.

deBree, G., 2010, Personal communication.

Essick, J., 2009, "Hands-On Introduction to LabVIEW for Scientists and Engineers," Oxford University Press, New York, NY.

Gillmer, T., and Johnson, B., 1982, "Introduction to Naval Architecture," Naval Institute Press, Annapolis, MD.

Hau, E., 2006, "Wind Turbines: Fundamentals, Technologies, Application, Economics," Springer, Berlin.

Holman, J.P., 2001, "Experimental Methods for Engineers," McGraw-Hill, New York, NY.

Lokocz, T., 2010, "Solid Mechanics of Cross Flow Tidal Turbine Blades," University of Maine.

Lokocz, T., 2011, Personal communication.

McAdam, R. A., Houlsby, G. T., Oldfield, M. L. G., and McCulloch, M. D., 2009, "Experimental Testing of the Transverse Horizontal Axis Water Turbine," Proceedings, 8th European Wave and Tidal Energy Conference, Uppsala, Sweden, pp. 360-365.

Migliore, P.G., and Wolfe, W.P., 1980, "The Effects of Flow Curvature on the Aerodynamics of Darrieus Wind Turbines," W.V.U. A.E. Report No. TR-60, West Virginia University, Morgantown, WV.

Meyer, R., 1999, "Introduction to mathematical Fluid Dynamics," Dover Publications, Inc., Mineola, NY.

Polagye, B., Van Cleve, B., Copping, A., Kirkendall, K., 2010, "Environmental Effects of Tidal Energy Development: Proceedings of a Scientific Workshop," U.S. Dept. Commerce, NOAA Tech. Memo. F/SPO-116, 181 p.

Schlichting, H., and Gersten, K., 2000, "Boundary Layer Theory," Springer, New York, NY.

Sheldahl, R.E., and Klimas, P.C., 1981, "Aerodynamic Characteristics of Seven Symmetrical Airfoil Sections Through 180-Degree Angle of Attack for Use in Aerodynamic Analysis of Vertical Axis Wind Turbines," Technical Report SAND80-2114, Sandia National Laboratories, Albuquerque, NM.

Shiono, M., Suzuki, K., and Kiho, S., 2000, "An Experimental Study of the Characteristics of a Darrieus Turbine for Tidal Power Generation," Electrical Engineering in Japan. Vol. 132, No. 3, pp. 38-47.

Strickland, J. H., Webster, B. T., and Nguyen, T., 1980, "A Vortex Model of the Darrieus Turbine: an Analytical and Experimental Study," Technical Report SAND79-7058, Sandia National Laboratories, Albuquerque, NM.

Urbina, R., Peterson, M.L., Kimball, R.W., DeBree, G.S., and Cameron, M.P., 2011a, "Modeling and Validation of a Cross Flow Turbine Using Free Vortex Model and a Modified Dynamic Stall Model," Submitted to: Renewable Energy.

Urbina, R., 2013, Personal communication.

Viehman, H., 2013, Personal communication.

Villeneuve, R., 1993, "Effects of Viscosity on Hydrofoil Cavitation," Massachusettes Institute of Technology.

Wallace, T., 2013, Personal communication.

Whelan, J. I., Graham, M.R., Peiro, J., 2009, Journal of Fluid Mechanics, Vol. 624, pp. 281-291.

White, F., 2011, "Fluid Mechanics," McGraw-Hill, New York, NY.

APPENDIX A

SCALING CALCULATIONS

Reynolds number scaling is not viable for the current test setup. With the model being considerably smaller than the prototype, the velocity of the model would have to reach speeds upwards of 23 m/s in order to have dynamic similitude, as shown by the calculations below. For the following calculations, the prototype was based off of the dimensions of Ocean Renewable Power Company's TidGen™ Turbine in the Cobscook Bay. Values of density and dynamic viscosity for the Cobscook Bay were determined based off of data from the National Oceanic and Atmospheric Administration (NOAA) based in Eastport, Maine and data collected by Viehman, 2012.

The Reynolds number for the prototype, Re_p, is calculated by Eq. A.1 where L_p is the length of the prototype diameter, V_p is the average inflow velocity of the Cobscook Bay, ρ_p is the density of the seawater, and μ_p is the dynamic viscosity of the seawater.

$$Re_p = \frac{\rho_p V_p L_p}{\mu_p} \tag{A.1}$$

$$Re_p = \frac{\left(1027.8 \frac{kg}{m^2}\right)(2.5 \frac{m}{s})(3.6576\ m)}{(0.001645\ N \cdot \frac{s}{m^2})}$$

$$Re_p = 5.71x10^6$$

To ensure dynamic similitude, set the prototype Reynolds number equal to the model Reynolds number and solve for the inflow velocity of the model. In Eq. A.1, L_m is the

length of the model diameter, V_m is the inflow velocity of the tow tank, ρ_p is the density of the water, and μ_m is the dynamic viscosity of the water.

$$Re_m = \frac{\rho_m V_m L_m}{\mu_m} \tag{A.2}$$

$$Re_p = Re_m = 5.71x10^6 = \frac{\left(1000\frac{kg}{m^3}\right)(V_m)(0.3302\ m)}{(0.001348\ N \cdot \frac{s}{m^2})}$$

$$V_m = 23.3\ \frac{m}{s}$$

This velocity was much too high for tow tank operations and therefore was not used for scaling. Froude number, however, scaled very closely as seen in the calculations from Eq. A.3 and Eq. A4 where V_p is the average inflow velocity of the Cobscook Bay, g is gravitational acceleration, L_p is the length of the prototype diameter, V_m is the inflow velocity of the tow tank, and L_m is the diameter of the model.

$$Fr_p = \frac{V_p}{\sqrt{gL_p}} \tag{A.3}$$

$$Fr_p = \frac{2.5\ \frac{m}{s}}{\sqrt{(9.81\frac{m}{s^2})(3.6576\ m)}}$$

$$Fr_p = 0.4174$$

$$Fr_m = \frac{V_m}{\sqrt{gL_m}} \tag{A.4}$$

$$Fr_p = Fr_m \frac{V_m}{\sqrt{(9.81 \frac{m}{s^2})(0.3302\ m)}}$$

$$V_m = 0.75\ \frac{m}{s} \approx 0.8\ \frac{m}{s}$$

By scaling with Froude number, the velocity was a more reasonable value that could be easily tested using the tow tank. As a result all testing was performed at an inflow velocity of 0.8 m/s.

APPENDIX B

EXPERIMENTAL TEST MATRIX

Toe Angle	Tip Speed Ratio (λ)													
	1	1.25	1.5	1.6	1.7	1.8	1.9	2.0	2.1	2.2	2.3	2.4	2.5	2.8
-3^0	X	X	X	X	X	X	X	X	X	X	X	X	X	X
-2^0	X	X	X	X	X	X	X	X	X	X	X	X	X	X
-1^0	X	X	X	X	X	X	X	X	X	X	X	X	X	X
0^0	X	X	X	X	X	X	X	X	X	X	X	X	X	X
$+1^0$	X	X	X	X	X	X	X	X	X	X	X	X	X	X
$+2^0$	X	X	X	X	X	X	X	X	X	X	X	X	X	X
$+3^0$	X	X	X	X	X	X	X	X	X	X	X	X	X	X
$+4^0$	X	X	X	X	X	X	X	X	X	X	X	X	X	X
$+5^0$	X	X	X	X	X	X	X	X	X	X	X	X	X	X
$+6^0$	X	X	X	X	X	X	X	X	X	X	X	X	X	X
$+7^0$	X	X	X	X	X	X	X	X	X	X	X	X	X	X
$+8^0$	X	X	X	X	X	X	X	X	X	X	X	X	X	X
$+9^0$	X	X	X	X	X	X	X	X	X	X	X	X	X	X
$+10^0$	X	X	X	X	X	X	X	X	X	X	X	X	X	X

Table B.1 – Experimental test matrix for two-bladed NACA 0018 foils at a water temperature of 67^0F with U_∞ = 0.8 m/s, σ = 0.171, and water column height at 40 inches.

Toe Angle	Tip Speed Ratio (λ)															
	0.4	0.5	0.6	0.7	0.8	0.9	1.0	1.1	1.2	1.3	1.4	1.5	1.6	1.7	1.8	1.9
-4^0	X	X	X	X	X	X	X	X	X	X	X	X	X	X	X	X
-3^0	X	X	X	X	X	X	X	X	X	X	X	X	X	X	X	X
-2^0	X	X	X	X	X	X	X	X	X	X	X	X	X	X	X	X
-1^0	X	X	X	X	X	X	X	X	X	X	X	X	X	X	X	X
0^0	X	X	X	X	X	X	X	X	X	X	X	X	X	X	X	X
$+1^0$	X	X	X	X	X	X	X	X	X	X	X	X	X	X	X	X
$+2^0$	X	X	X	X	X	X	X	X	X	X	X	X	X	X	X	X
$+3^0$	X	X	X	X	X	X	X	X	X	X	X	X	X	X	X	X
$+4^0$	X	X	X	X	X	X	X	X	X	X	X	X	X	X	X	X
$+5^0$	X	X	X	X	X	X	X	X	X	X	X	X	X	X	X	X
$+6^0$	X	X	X	X	X	X	X	X	X	X	X	X	X	X	X	X
$+7^0$	X	X	X	X	X	X	X	X	X	X	X	X	X	X	X	X
$+8^0$	X	X	X	X	X	X	X	X	X	X	X	X	X	X	X	X
$+9^0$	X	X	X	X	X	X	X	X	X	X	X	X	X	X	X	X
$+10^0$	X	X	X	X	X	X	X	X	X	X	X	X	X	X	X	X

Table B.2 – Experimental test matrix for four-bladed NACA 0018 foils at a water temperature of 67^0F with U_∞ = 0.8 m/s, σ = 0.343, and water column height at 40 inches.

The test matrix for the symmetrical NACA 0018 foils was repeated for two-bladed testing during the winter in order to provide comparable results to the cambered NACA 4418 and reverse cambered NACA 4418 tests (Fig. B.3). Compressed experimental test matrices were developed to provide a curve with refinement at the peak power coefficient.

Toe Angle	Tip Speed Ratio (λ)															
	0.4	0.5	0.6	0.7	0.8	0.9	1.0	1.1	1.2	1.3	1.4	1.5	1.6	1.7	1.8	1.9
-4^0	X	X	X	X	X	X	X	X	X	X	X	X	X	X	X	X
-2^0	X	X	X	X	X	X	X	X	X	X	X	X	X	X	X	X
0^0	X	X	X	X	X	X	X	X	X	X	X	X	X	X	X	X
$+3^0$	X	X	X	X	X	X	X	X	X	X	X	X	X	X	X	X
$+4^0$	X	X	X	X	X	X	X	X	X	X	X	X	X	X	X	X
$+5^0$	X	X	X	X	X	X	X	X	X	X	X	X	X	X	X	X
$+6^0$	X	X	X	X	X	X	X	X	X	X	X	X	X	X	X	X
$+7^0$	X	X	X	X	X	X	X	X	X	X	X	X	X	X	X	X
$+10^0$	X	X	X	X	X	X	X	X	X	X	X	X	X	X	X	X

Table B.3 – Experimental test matrix for two-bladed NACA 0018 foils at a water temperature of 48^0F with U_∞ = 0.8 m/s, σ = 0.343, and water column height at 40 inches.

Toe Angle	Tip Speed Ratio (λ)															
	0.4	0.5	0.6	0.7	0.8	0.9	1.0	1.1	1.2	1.3	1.4	1.5	1.6	1.7	1.8	1.9
-4^0	X	X	X	X	X	X	X	X	X	X	X	X	X	X	X	X
-2^0	X	X	X	X	X	X	X	X	X	X	X	X	X	X	X	X
0^0	X	X	X	X	X	X	X	X	X	X	X	X	X	X	X	X
$+3^0$	X	X	X	X	X	X	X	X	X	X	X	X	X	X	X	X
$+4^0$	X	X	X	X	X	X	X	X	X	X	X	X	X	X	X	X
$+5^0$	X	X	X	X	X	X	X	X	X	X	X	X	X	X	X	X
$+6^0$	X	X	X	X	X	X	X	X	X	X	X	X	X	X	X	X
$+7^0$	X	X	X	X	X	X	X	X	X	X	X	X	X	X	X	X
$+10^0$	X	X	X	X	X	X	X	X	X	X	X	X	X	X	X	X

Table B.4 – Experimental test matrix for two-bladed cambered NACA 4418 foils at a water temperature of 48^0F with U_∞ = 0.8 m/s, σ = 0.171, and water column height at 40 inches.

Toe Angle	Tip Speed Ratio (λ)														
	0.6	0.8	1.0	1.1	1.2	1.3	1.4	1.5	1.6	1.7	1.8	1.9	2.0	2.2	2.4
0^0	X	X	X	X	X	X	X	X	X	X	X	X	X	X	X
$+2^0$	X	X	X	X	X	X	X	X	X	X	X	X	X	X	X
$+3^0$	X	X	X	X	X	X	X	X	X	X	X	X	X	X	X
$+4^0$	X	X	X	X	X	X	X	X	X	X	X	X	X	X	X
$+5^0$	X	X	X	X	X	X	X	X	X	X	X	X	X	X	X
$+6^0$	X	X	X	X	X	X	X	X	X	X	X	X	X	X	X
$+7^0$	X	X	X	X	X	X	X	X	X	X	X	X	X	X	X
$+8^0$	X	X	X	X	X	X	X	X	X	X	X	X	X	X	X
$+9^0$	X	X	X	X	X	X	X	X	X	X	X	X	X	X	X
$+10^0$	X	X	X	X	X	X	X	X	X	X	X	X	X	X	X

Table B.5 – Experimental test matrix for two-bladed reverse cambered NACA 4418 foils at a water temperature of 48^0F with $U_\infty = 0.8$ m/s, $\sigma = 0.171$, and water column height at 40 inches.

APPENDIX C

EFFECTS OF TEMPERATURE

Initial testing was done in the summer months where the water temperature was 67^0F. When further data was taken at a water temperature of 48^0F, there was a noticeable change in turbine performance. Looking at the most efficient blades, the symmetrical NACA 0018 profile, a decrease is seen over the whole performance curve. The results shown in Fig. C.1 are for two-bladed testing of the symmetrical NACA 0018 foils set at the most efficient toe angle, $+6^0$, and inflow velocity of 0.8 m/s. The water column height was set at 42 inches with the turbine centered in the water column. Effects of water column height on turbine performance are explained in Appendix D.

The winter results were less efficient than the summer results by an average of approximately 4% over the entire curve. The summer experimental tests, as shown in chapter 3, had a peak efficiency of 42.2% where the winter tests peaked at 37%. Since temperature is the only changing variable in this study, it can be concluded that the change in fluid viscosity is responsible for this reduction. If the effects of viscous forces are not taken into account during design, boundary separation can occur which can result in an increase in drag and decrease in lift as seen in the results here.

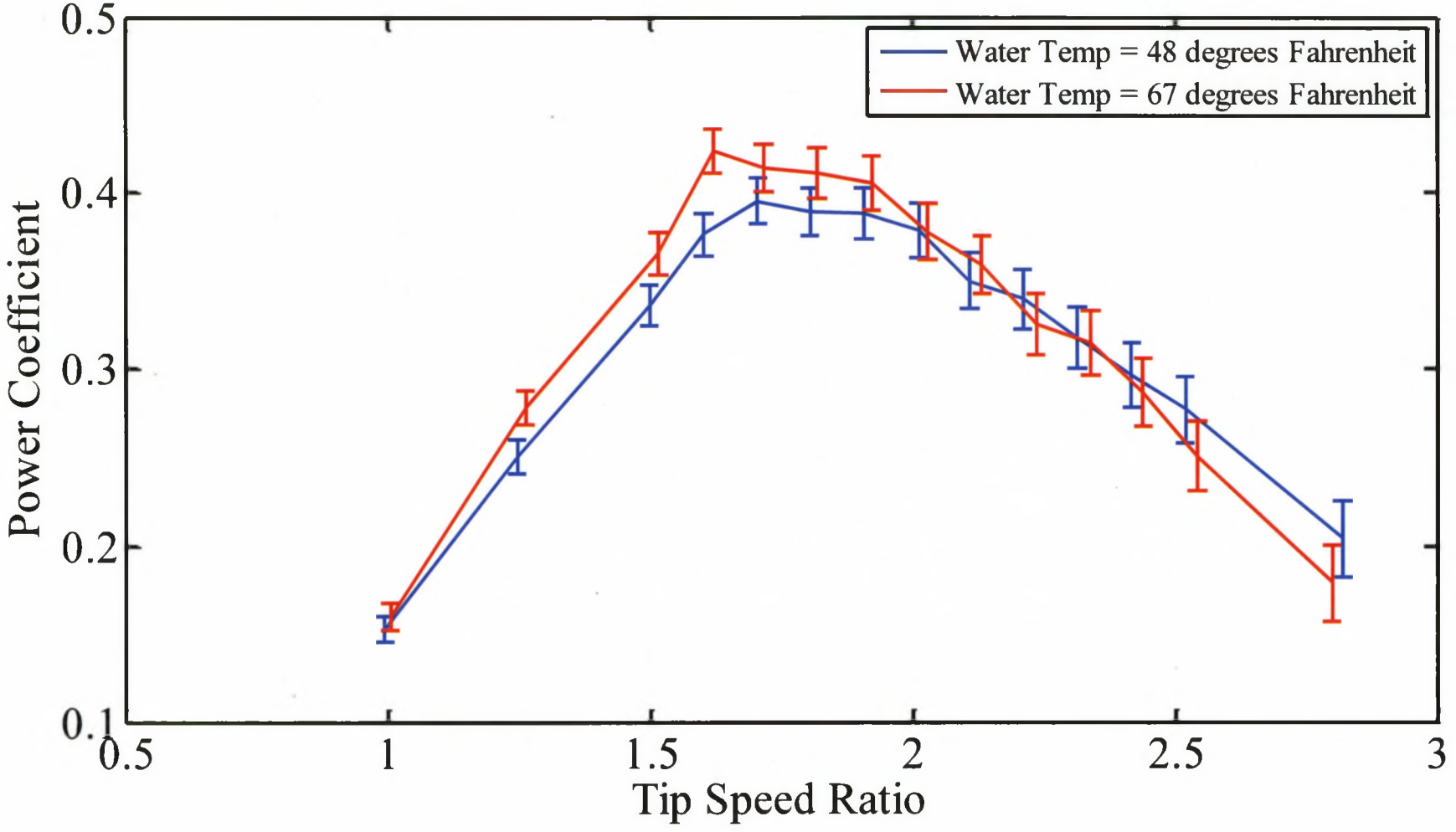

Figure C.1 – Comparison of power coefficient curves for two-blade testing of 3-D printed NACA 0018 blades at $+6^0$ toe angle. Testing was performed at 67^oF (Re = 258115) and 48^oF (Re = 193886) with solidity ratio $\sigma = 0.171$ and inflow velocity $U_\infty = 0.8$ m/s.

APPENDIX D

EFFECTS OF WATER COLUMN HEIGHT

During testing it was observed that a change in water column height can drastically change turbine performance. The power coefficient may be influenced by the distance of the turbine to the free surface or bottom of the tank because the presence of a boundary can cause flow acceleration above and below the turbine (Adamski, 2013). The series of experiments listed in Table C.1 show the tests performed at a variation of water column heights. The turbine remained stationary with the center at a distance of 20 inches from the bottom of the tank as it was in all testing. Tests were taken at a short range of tip speed ratios to capture the peak power coefficient.

Water Column Height	Tip Speed Ratio (λ)							
	1.5	1.6	1.7	1.8	1.9	2.0	2.1	2.2
30"	X	X	X	X	X	X	X	X
32"	X	X	X	X	X	X	X	X
34"	X	X	X	X	X	X	X	X
36"	X	X	X	X	X	X	X	X
38"	X	X	X	X	X	X	X	X
40"	X	X	X	X	X	X	X	X
42"	X	X	X	X	X	X	X	X
44"	X	X	X	X	X	X	X	X

Table D.1 - Experimental test matrix for two-bladed NACA 0018 foils at water column heights from 30 to 44 inches in two degree increments. Toe angle was set to $+6^0$, solidity $\sigma = 0.171$, and inflow velocity $U_\infty = 0.8$ m/s.

The water column height was nondimentionalized in Figure D.1 through a ratio of the water height from the center of the turbine to the free surface compared to the turbine radius.

Since the testing was performed in the tow tank in a constricted flow, the blockage effect has a large amount of influence on performance results (McAdam et al., 2009). The blockage effect is quantified by determining the blockage ratio (BR) from Eq. D.1 where A_t is the cross sectional area of the turbine and A_c is the cross sectional area of the channel.

$$BR = \frac{A_t}{A_c} \tag{D.1}$$

Under these conditions, the constricted flow causes flow acceleration around the turbine which changes the apparent inflow velocity. As a result, the actual measured inflow velocity is lower than the apparent inflow velocity and the power coefficient is artificially high. By reducing the blockage ratio, the effect on the power coefficient is reduced (McAdam et al., 2009).

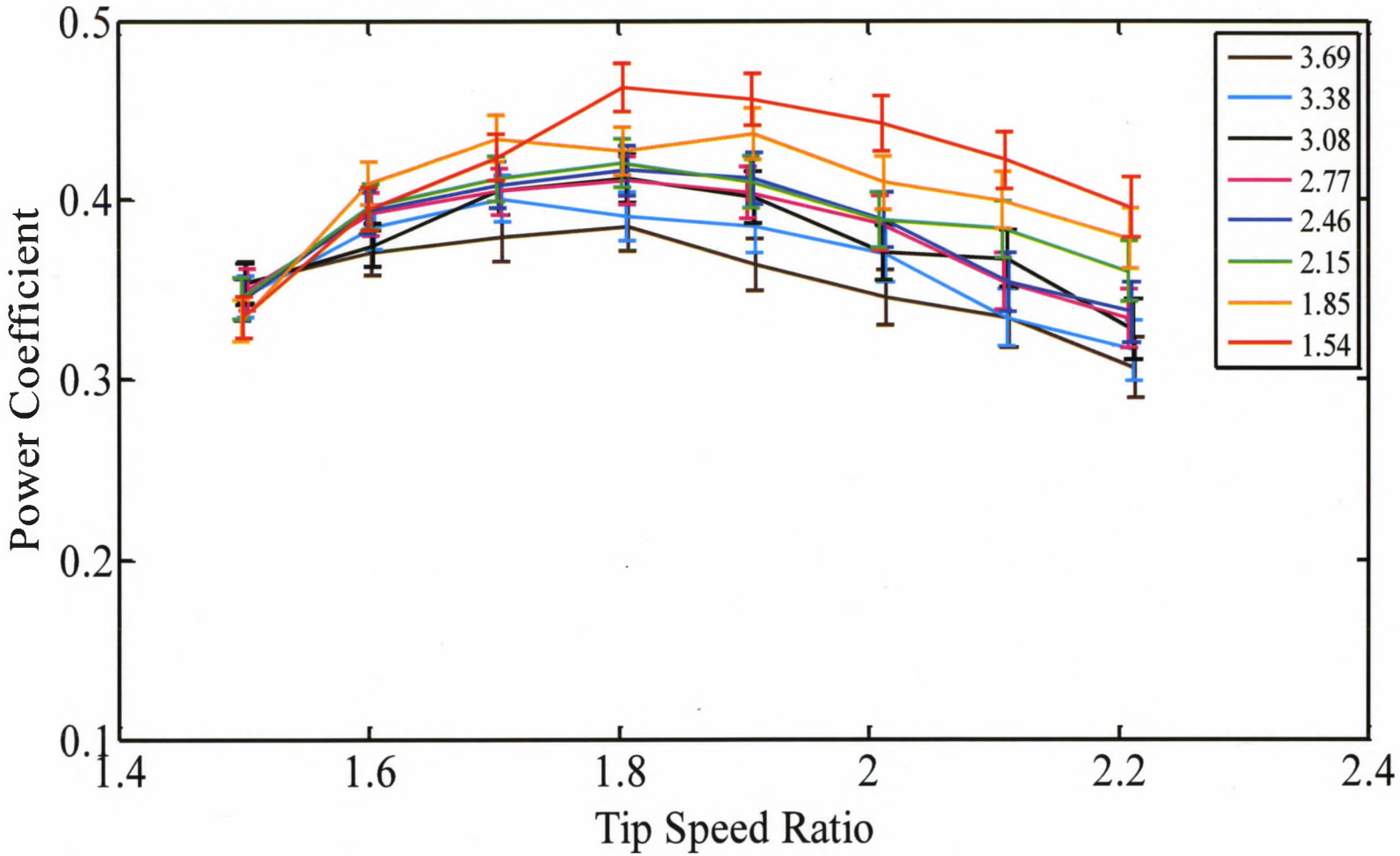

Figure D.1 – Comparison of power coefficient curves for two-blade testing of 3-D printed NACA 0018 blades at +6° toe angle for varying water column height. The center of the turbine was kept at 20 inches from the bottom of the tank. Testing was performed at 48°F with solidity ratio $\sigma = 0.171$ and inflow velocity $U_\infty = 0.8$ m/s.

APPENDIX E

FILTERING METHODS

Angular velocity of the turbine was calculated by using data collected by angular position using an encoder. Angular position is recorded from 0 to 360 degrees, after which it resets to zero again. This causes the sawtooth output seen in the figures below. Due to the noise seen in bottom portion of Figure E.1, filtering was required following the removal of the discontinuity related to the reset of the encoder upon each revolution.

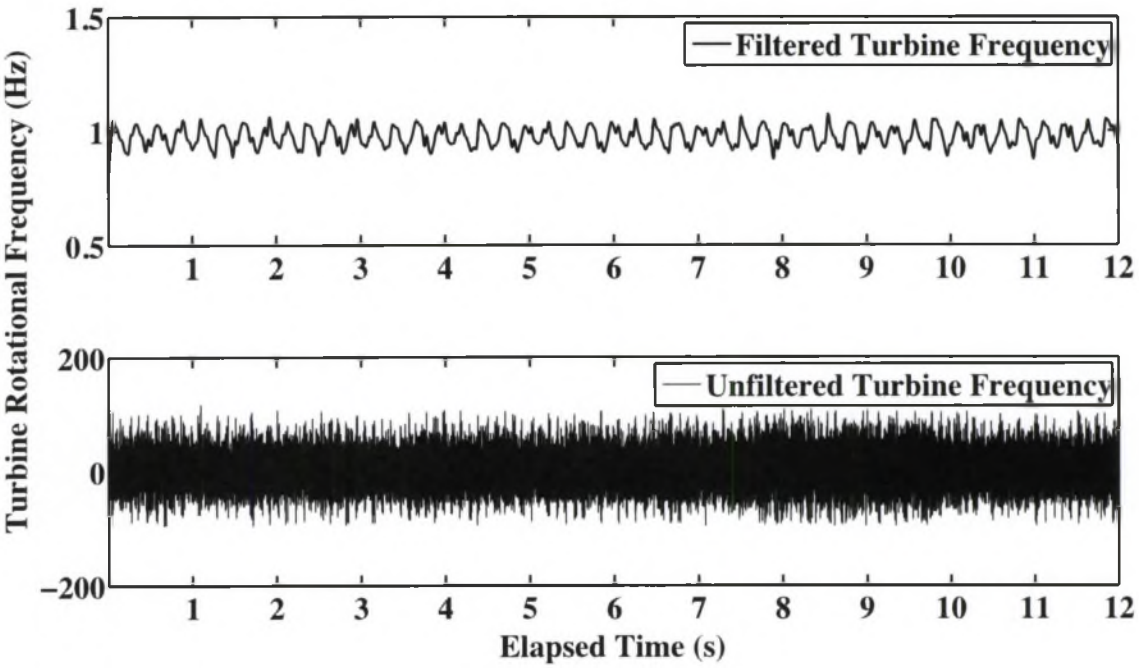

Figure E.1 – Comparison of filtered and unfiltered turbine frequency in Hz over time (Image source: deBree, 2010)

The sawtooth data from Figure E.2 was modified to a straight line by converting to radians, detecting the peak values, then adding multiples of 2π accordingly. Once discontinuities were eliminated, coefficients were created for a finite impulse response

linear-phase low pass filter with a Hamming window using standard MATLAB software functions. For the turbine rotational frequency, a cut-off frequency of 8 Hz was selected.

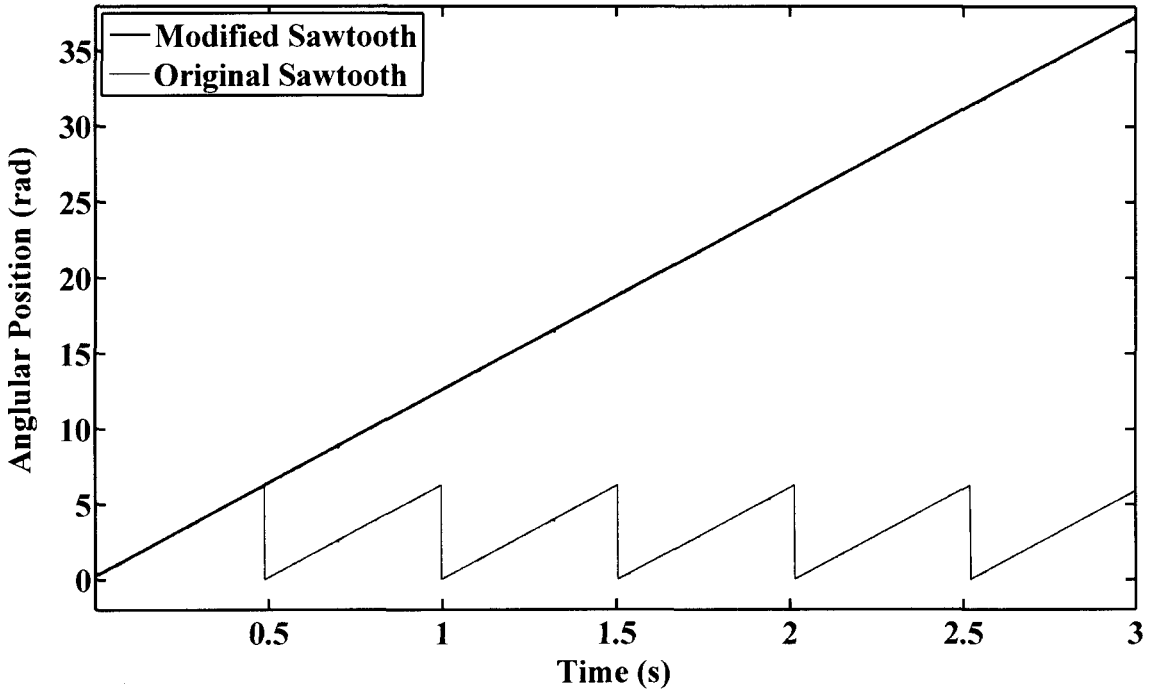

Figure E.2 – Angular position output from the turbine encoder over time displayed as the original sawtooth and the modified sawtooth used to eliminate discontinuities (Image source: deBree, 2010)

This same low pass filter was used to filter the torque data after a small change in the cut-off frequency to 17 Hz. This cut-off frequency is just a bit lower than the natural frequency of the system. Testing showed that altering the cut-off frequency had very little effect on change in the power coefficient. Comparison of the unfiltered and filtered torque data is shown in Figure E.3.

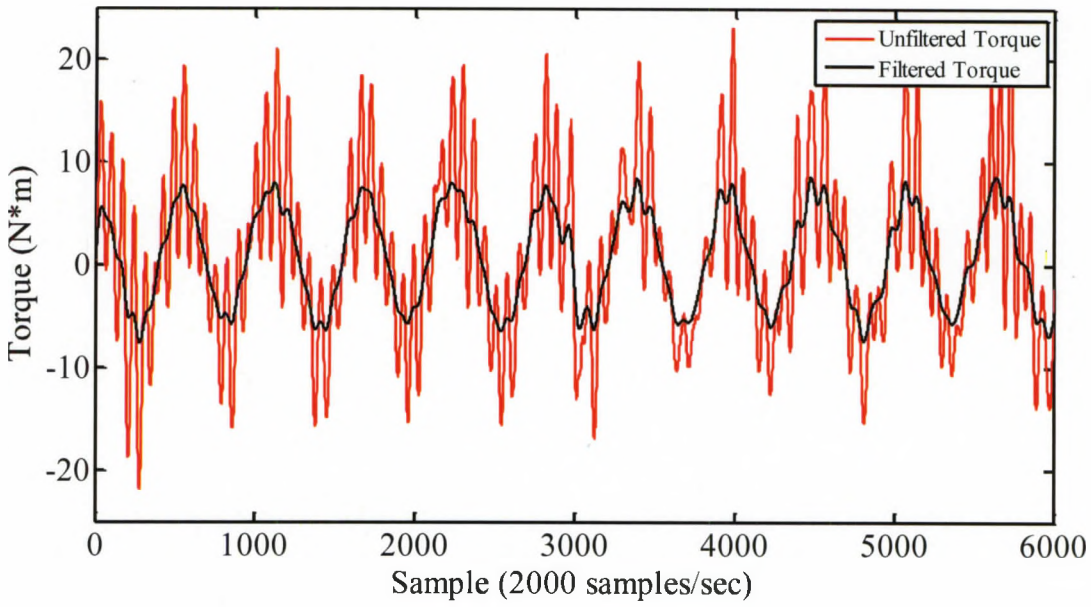

Figure E.3 – Comparison of filtered and unfiltered torque for NACA 0018 foils at $+6^0$ toe angle, 0.8 m/s inflow velocity, and TSR of 1.5.

BIOGRAPHY OF THE AUTHOR

Megan Colleen Swanger from Springvale, Maine graduated from Sanford High School in 2002. She went on to attend Norwich University, the Military College of Vermont, where she graduated with a B.S. in Mechanical Engineering in 2006. After graduating, she commissioned into the United States Army as a second lieutenant on active duty. She spent three years traveling around the United States and abroad as a chemical officer. After returning from her deployment to Iraq in 2009, she was promoted to captain and decided to leave active duty in 2010 to attend graduate school. She currently is serving in the Maine Army National Guard as the company commander for the 185th Engineer Support Company. She is a candidate for the Master of Science degree in Mechanical Engineering from the University of Maine in August, 2013.